White Rose Research Online

eprints@whiterose.ac.uk
https://eprints.whiterose.ac.uk
Universities of Leeds, Sheffield and York

Deposited via The University of Leeds.

White Rose Research Online URL for this paper:
https://eprints.whiterose.ac.uk/id/eprint/188150/

Version: Published Version

---

**Article:**
Zamponi, J, Maureira, MJ, Zhao, B et al. (2021) The young protostellar disc in IRAS 16293−2422 B is hot and shows signatures of gravitational instability. Monthly Notices of the Royal Astronomical Society, 508 (2). pp. 2583-2599. ISSN: 0035-8711

https://doi.org/10.1093/mnras/stab2657

---

This article has been published in Monthly Notices of the Royal Astronomical Society ©:2021 The Author(s) Published by Oxford University Press on behalf of the Royal Astronomical Society. All rights reserved.

**Reuse**
Items deposited in White Rose Research Online are protected by copyright, with all rights reserved unless indicated otherwise. They may be downloaded and/or printed for private study, or other acts as permitted by national copyright laws. The publisher or other rights holders may allow further reproduction and re-use of the full text version. This is indicated by the licence information on the White Rose Research Online record for the item.

**Takedown**
If you consider content in White Rose Research Online to be in breach of UK law, please notify us by emailing eprints@whiterose.ac.uk including the URL of the record and the reason for the withdrawal request.

Monthly Notices
of the
ROYAL ASTRONOMICAL SOCIETY

MNRAS **508,** 2583–2599 (2021)
Advance Access publication 2021 September 20

https://doi.org/10.1093/mnras/stab2657

# The young protostellar disc in IRAS 16293−2422 B is hot and shows signatures of gravitational instability

Joaquin Zamponi [1]★ María José Maureira [1] Bo Zhao [1] Hauyu Baobab Liu,[2] John D. Ilee [3] Duncan Forgan [4] and Paola Caselli[1]

[1]*Max-Planck-Institut für Extraterrestrische Physik (MPE), D-85748 Garching, Germany*
[2]*Institute of Astronomy and Astrophysics, Academia Sinica, 11F of Astronomy-Mathematics Building, AS/NTU No.1, Section 4, Roosevelt Rd, Taipei 10617, Taiwan, ROC*
[3]*School of Physics and Astronomy, University of Leeds, Leeds LS2 9JT, UK*
[4]*Centre for Exoplanet Science, SUPA, School of Physics & Astronomy, University of St Andrews, St Andrews KY16 9SS, UK*

Accepted 2021 September 13. Received 2021 September 13; in original form 2021 April 26

## ABSTRACT

Deeply embedded protostars are actively fed from their surrounding envelopes through their protostellar disc. The physical structure of such early discs might be different from that of more evolved sources due to the active accretion. We present 1.3 and 3 mm ALMA continuum observations at resolutions of 6.5 and 12 au, respectively, towards the Class 0 source IRAS 16293−2422 B. The resolved brightness temperatures appear remarkably high, with $T_b > 100$ K within ∼30 au and $T_b$ peak over 400 K at 3 mm. Both wavelengths show a lopsided emission with a spectral index reaching values less than 2 in the central ∼20 au region. We compare these observations with a series of radiative transfer calculations and synthetic observations of magnetohydrodynamic and radiation hydrodynamic protostellar disc models formed after the collapse of a dense core. Based on our results, we argue that the gas kinematics within the disc may play a more significant role in heating the disc than the protostellar radiation. In particular, our radiation hydrodynamic simulation of disc formation, including heating sources associated with gravitational instabilities, is able to generate the temperatures necessary to explain the high fluxes observed in IRAS 16293B. Besides, the low spectral index values are naturally reproduced by the high optical depth and high inner temperatures of the protostellar disc models. The high temperatures in IRAS 16293B imply that volatile species are mostly in the gas phase, suggesting that a self-gravitating disc could be at the origin of a hot corino.

**Key words:** radiative transfer – protoplanetary discs – stars: protostars.

## 1 INTRODUCTION

In the earliest stages of star formation, the Class 0 stage (Andre, Ward-Thompson & Barsony 2000), the protostellar envelope still contains a significant fraction of the total mass of the system. The protostellar disc is continuously fed by the surrounding envelope and it may become gravitationally unstable depending on environmental conditions at the start of the pre-stellar core collapse (e.g. Zhao et al. 2018). Large streamers of molecular material from the outer envelope and surrounding cloud can also contribute to the disc mass growth (Akiyama et al. 2019; Dullemond et al. 2019; Kuffmeier et al. 2020; Pineda et al. 2020). Gravitationally unstable discs can fragment, enabling the formation of giant planets (Boss 2009; Vorobyov & Basu 2010; Machida, Inutsuka & Matsumoto 2011) and develop spiral arms where gas compression and shocks locally heat the gas and dust to values well above those predicted by irradiated viscously evolving discs (e.g. Boley & Durisen 2008; Dong et al. 2016). The chemical composition of the disc is heavily affected by gravitational instabilities (GIs; e.g. Ilee et al. 2011, 2017). Moreover, their relatively large masses and surface mass densities of gravitationally unstable discs imply large opacities of their dust emission at millimetre and submillimetre wavelengths, thus hindering total mass measurements (e.g. Evans et al. 2017; Li et al. 2017; Galván-Madrid et al. 2018) and making molecular line observations difficult to probe their full structure (Evans et al. 2019).

So far, there is no clear evidence of a gravitational unstable disc among Class 0 sources, with the possible exception of the disc around the triple protostar system L1448 IRS3B (Tobin et al. 2016), but this disc is highly perturbed by the presence of multiple sources which can induce tidal forces and instabilities mimicking original GIs. To make progress in this field and unveil a gravitationally unstable disc at the earliest stages of star formation, one needs high sensitivity and high angular resolution observations of a bright Class 0 source and state-of-the art numerical simulations of disc formation which can then be compared in detail with observations.

Located in the star-forming region $\rho$-Ophiuchi, inside the dark cloud L1689N and at a distance of 141 pc (Dzib et al. 2018), IRAS16293−2422 is a well-studied Young Stellar Object (YSO) classified as a Class 0 source with less than $10^4$ yr (Andre, Ward-Thompson & Barsony 1993), and represents one of the very early stages of low-mass star formation. It was the first source identified as a hot corino (Blake et al. 1994; van Dishoeck et al. 1995) based

★ E-mail: jzamponi@mpe.mpg.de

© 2021 The Author(s)
Published by Oxford University Press on behalf of Royal Astronomical Society

Downloaded from https://academic.oup.com/mnras/article/508/2/2583/6372913 by University of Leeds user on 28 June 2022

on the detection of Complex Organic Molecules (COMs) in the source, which was later supported by follow-up studies (Ceccarelli et al. 1998, 2000; Schöier et al. 2002; Crimier et al. 2010; Jørgensen et al. 2011, 2016; Pineda et al. 2012; Oya et al. 2016; Jacobsen et al. 2018; van der Wiel et al. 2019). Higher resolution observations revealed that IRAS16293−2422 is in fact a triple system, composed of sources A1 and A2, separated by 54 au from each other (Maureira et al. 2020) and source B, 738 au (5 arcse; Wootten 1989) away from source A. Due to this larger separation, tidal truncation between the three protostars is discarded and therefore source B is considered to have evolved as an isolated source (Rodríguez et al. 2005). It was initially proposed to be either an evolved T Tauri star (Stark et al. 2004; Takakuwa et al. 2007) or a very young object (Chandler et al. 2005), however, Chandler et al. (2005) suggested that source B has large-scale infalls based on SO line emission. Pineda et al. (2012) confirmed the infall of an inner envelope, with mass accretion rates of $4.5 \times 10^{-5}$ $M_{\odot}yr^{-1}$, based on ALMA detections of inverse P-Cygni profiles in $CH_3OCHO$-E, $CH_3OCHO$-E-A and $H_2CCO$, ruling out the possibility of it being a T Tauri star. The interpretations of infall from these profiles was also suggested by Jørgensen et al. (2012) and Zapata et al. (2013). Unlike the A1 and A2 protostars, source B has not shown clear signs of outflow launching, explained by the lack of free–free emission at low frequencies (Chandler et al. 2005; Rodríguez et al. 2005; Loinard et al. 2007; Rao et al. 2009; Liu et al. 2018; Hernández-Gómez et al. 2019b) and also based on molecular lines (Loinard et al. 2002; van der Wiel et al. 2019).

The possibility of source B being gravitationally unstable in the outer part of its disc was also proposed by Rodríguez et al. (2005) and discussed by Kratter & Lodato (2016). The disc around source B must be highly dense and massive ($\gtrsim$0.2 $M_{\odot}$; Rao et al. 2009; Pineda et al. 2012) to produce gravitational instabilities. After comparing high-sensitivity interferometric data with MHD and RHD star formation simulations, we demonstrate here that indeed the physical structure (in particular the temperature) of the IRAS16293−2422 B disc resembles that of a self-gravitating disc.

This paper is organized as follows: in Section 2 we provide details on the data observation and reduction, followed by our results from the ALMA observations, in Section 3 we describe the numerical simulations used to compare against our ALMA observations, in Section 4 we outline the post-processing scheme done with radiative transfer calculations, in Section 5 we compare our synthetic observations to the real data, then we discuss about possible interpretations for the features observed in Section 6 and finally, we present our conclusion in Section 7.

## 2 OBSERVATIONS

### 2.1 Data and imaging

Observations of IRAS 1629−2422 were taken in band 3 and band 6 with ALMA (project IDs: 2017.1.01247.S and 2016.1.00457.S, respectively). The band 3 observations were taken on 2017 October 8 and 12 in the most extended Cycle 5 configuration with a baseline range of 41.4 m to 16.2 km and a maximum recoverable scale of ∼0.5 arcsec (or 70 au). The single spectral window for the band 3 continuum used in this work has a bandwidth of 2 GHz divided into 128 channels and centred at 99.988 GHz. The band 6 observations were taken during 2017 August 21. The baselines range between 21 and 3697 m, with a maximum recoverable scale of ∼0.6 arcsec (or 85 au). The spectral set-up consisted of four spectral windows centred at frequencies of 240.3, 240.5, 224.7, and 222.9 GHz, with channel widths of 61.0, 15.3, 30.5, and 488.3 kHz and bandwidths of 0.23, 0.06, 0.11, and 0.94 GHz, respectively. To create the continuum image we carefully check each spectral window and flag the lines. The resulting bandwidth for the band 6 continuum is 0.12 GHz with most of the channels coming from the spectral window centred at 222.9 GHz. Both, the band 3 and band 6 continuum data have been previously published in Maureira et al. (2020) and Oya & Yamamoto (2020), respectively.

For band 3, the procedure for the calibration of the continuum data (including phase and amplitude self-calibration) as well as the imaging is detailed in Maureira et al. (2020). In summary, when imaging the continuum we iteratively performed phase-only self-calibration with a minimum solution interval of 9 s. Afterwards we performed two amplitude self-calibration iterations, with a minimum solution interval of 60 s. The final continuum data set after phase + amplitude self-calibration was imaged using the `TCLEAN` task from the Common Astronomy Software Applications (CASA; v5.6.2) with the multiscale deconvolver (Cornwell 2008; Rau & Cornwell 2011) and a robust parameter of 0.5. The beam size, beam position angle (P.A.) and noise of the continuum image are 0.048 arcsec × 0.046 arcsec (6.5 au), 79.3° and 15 $\mu$Jy beam$^{-1}$, respectively. This image was used when analysing the band 3 data alone, while a new additional map was done for producing a spectral index map (see below). For band 6, we performed iteratively phase-only self-calibration with a minimum solution interval of `SOLINT = 'INT'` or 4 s. Afterwards we performed one amplitude self-calibration, with`SOLINT = 'INF'` (two solutions, one for each track). For the process of self-calibration of the final image we selected visibilities with a minimum baseline of 120 $k\lambda$, in order to avoid missing flux artefacts, but also because shorter baselines are not covered by the band 3 observations with which we want to compare for our analysis.

The continuum image for band 6 and an additional continuum image for band 3 with matching *uv*-range were created using `TCLEAN`. This additional image of the band 3 data with matching *uv*-range was done with the goal of producing a spectral index map. We use multiscale, a robust parameter of 0 and a *uv*-range parameter of 120–2670 $k\lambda$ (overlapping baselines) for both data sets. Reference frequencies of 223 and 100 GHz were set for the band 6 and band 3 observations, respectively. The resultant beam size, P.A., and rms of the band 3 observations correspond to 0.062 arcsec × 0.050 arcsec, 41.7°, and 17 $\mu$Jy beam$^{-1}$, respectively. Similarly, for the band 6 observations these values are 0.114 arcsec × 0.069 arcsec, −88.2°, and 104 $\mu$Jy beam$^{-1}$, respectively. This study focuses on source B, corresponding to the single northern source of the IRAS 16293−2422 triple system. The corresponding maps for the southern pair (A1 and A2), as well as further details of the imaging in both bands, will be presented in Maureira et al. (in preparation).

### 2.2 Results

#### *2.2.1 Continuum observations at 1.3 and 3 mm*

The continuum observations obtained with ALMA towards source B are shown in Fig. 1 at $\lambda = 1.3$ and 3 mm. The structure seen at 3 mm has a radius of ∼46 au, measured along the major axis of a contour at $5\sigma$. This size is consistent with the reported typical sizes of embedded discs (Segura-Cox et al. 2018; Maury et al. 2019; Tobin et al. 2020) and also consistent with previous observations of this source (Rodríguez et al. 2005; Oya et al. 2018).

Interestingly, both wavelengths show the emission peak clearly shifted to the West of the centre of the overall structure. At a first



Downloaded from https://academic.oup.com/mnras/article/508/2/2583/6372913 by University of Leeds user on 28 June 2022

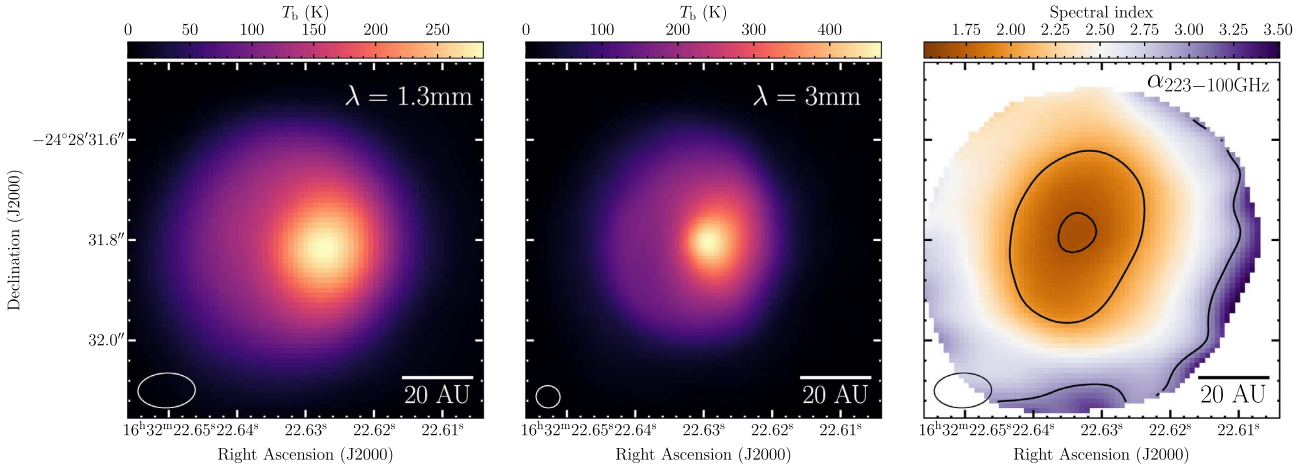


**Figure 1.** ALMA observations of IRAS16293−2422B. The left and central panels show the brightness temperatures observed at 1.3 mm (100 GHz; band 6) and 3 mm (223 GHz; band 3), respectively. The observation at 3 mm reports brighter emission than at 1.3 mm, with a peak value of $T_b \sim 470$ K and $T_b \sim 290$ K, respectively. Both images indicate the presence of a resolved brightness asymmetry in the source. The rightmost panel shows the spectral index calculated between the two wavelengths (as described in Appendix A), for which the 3 mm image was smoothed to match the 1.3 mm beam. Contours for the spectral index map are shown at 1.7, 2, and 3, inside-out. The synthesized beams are 0.114 arcsec × 0.069 arcsec and 0.048 arcsec × 0.046 arcsec at 1.3 and 3 mm (see bottom left corners).

glance, this shift could imply a possible inclination of the disc or the presence of a real asymmetry in density and/or temperature. The aspect ratio of the disc is ∼0.95 (derived from the east–west over north–south extensions of source B outlined by a contour at $5\,\sigma$). The ratio was measured in the optically thinner 3 mm image which, under the assumption of a circular disc, suggests a moderate inclination of ∼18°. If the disc were instead highly inclined, it would be expected that the peak would be more centred when seen at longer wavelengths. However, hints of a shift were also seen in high-resolution VLA continuum observations at 42 GHz reported by Rodríguez et al. (2005) and Hernández-Gómez et al. (2019b), unlike what is seen in the case of the highly inclined disc in HH212 (Lin et al. 2021). Furthermore, the line emission from complex organic molecules from the ALMA-PILS survey also appears to show a peak shifted to the west (Calcutt et al. 2018a, b; Manigand et al. 2020, 2021). Likewise, the source does not show a significant gradient indicative of rotation in previous ALMA line observations from 100 au down to 70 au scales. Instead, the kinematics is consistent with mostly infall motions (Pineda et al. 2012; Zapata et al. 2013; Oya et al. 2018) in a system with a face-on disc. All the above evidence suggests that there might be a real asymmetry present in the temperature and/or density structure of source B, instead of being a product of optical depth and inclination.

The brightness temperatures and rms uncertainties in the position of the peak are $T_b^{1.3mm} = 287 \pm 0.3$ K and $T_b^{3mm} = 470 \pm 1$ K, with the 3mm one remaining higher than the 1.3 mm even after smoothing the 3mm observations to match the beam of the 1.3 mm observations ($T_{b,\,smooth}^{3mm} = 364 \pm 0.4$ K). This same trend, of higher brightness temperature for longer wavelengths, is also consistent with recent VLA observations at 41 GHz (7 mm) and 33 GHz (9 mm) in Hernández-Gómez et al. (2019b), which had a comparable resolution to our observations. They measured a peak brightness of $T_b^{7mm} = 870$ K and $T_b^{9mm} = 700$ K. Additionally, they reported ALMA observations at 700 GHz that have a brightness temperature of $T_b^{1mm} = 185$ K. This trend is consistent with self-obscuration of inner hot material due to high optical depth, a scenario that we investigate in Section 5.2 and discuss in Section 6.1.

### 2.2.2 *Spectral index*

We derived the spectral index $\alpha$ between our ALMA observations at 1.3 and 3 mm using equation (A1). For this, we use maps imaged using the same *uv*-range (Section 2.1) and smoothing afterwards to match beams. The results are shown on the rightmost panel of Fig. 1. Black contours are placed at $\alpha = 1.7$, 2, and 3, inside-out. A clear decrease of spectral index is observed towards the centre, ranging from 3 to values as low as 1.7. The middle contour, at $\alpha = 2$, shows an elongated shape. A similarly low $\alpha$ was measured in the centre by Loinard et al. (2007) and it was suggested to be due to a modest thermal jet. However, Hernández-Gómez et al. (2019b) compiled integrated fluxes using SMA, VLA, and ALMA observations ranging from 3 to 700 GHz and found no evidence of free–free emission. The SED was well fitted with a single spectral index of $\alpha = 2.28 \pm 0.02$, in agreement with optically thick thermal dust emission at all wavelengths.

Spectral indices close to and lower than 2 have also been reported towards other sources, such as those in the PROSAC survey of Class 0/I protostars (Jørgensen et al. 2007, 2009) and also towards the Class I source WL12 (Miotello et al. 2014). More recently, Lin et al. (2021) presented a map of the spectral index between ALMA bands 3, 6, and 7 towards the embedded edge-on disc around the Class 0 protostar HH212. The spectral index reaches values as low as ∼1.5 within the central ∼50 ($\alpha_{band\,3,6}$) and 80 au ($\alpha_{band\,6,7}$). The observations were well reproduced by considering a temperature gradient increasing towards the inner regions of the disc, which under optically thick conditions, results in self-obscuration of the inner hot regions and thus in low spectral indexes, as also suggested by Li et al. (2017) and Galván-Madrid et al. (2018). In section 6.1, we discuss further the origin of the low spectral index in source B, based on comparison with protostellar disc models formed from the collapse of a dense core.

Downloaded from https://academic.oup.com/mnras/article/508/2/2583/6372913 by University of Leeds user on 28 June 2022

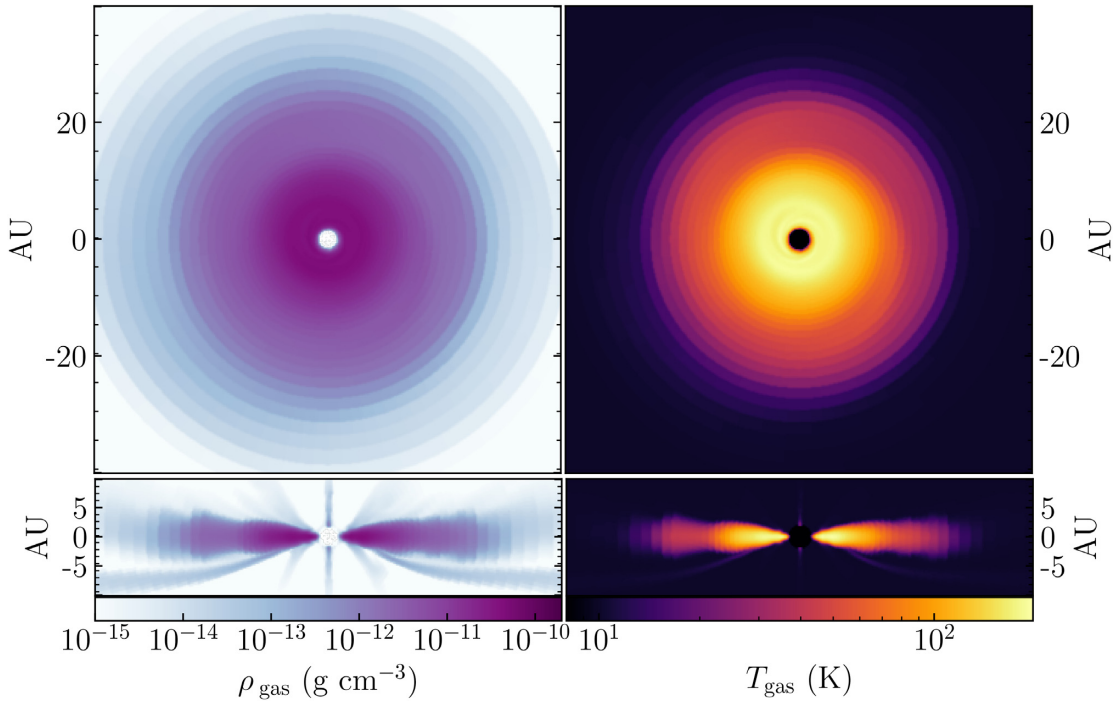


**Figure 2.** Face- and edge-on slices of the gas density (left-hand column) and gas temperature (right-hand column) distributions for the MHD disc model from Zhao et al. (2018), as described in Section 3.1.1.

## 3 PROTOSTELLAR DISC SIMULATIONS

### 3.1 Simulations of disc formation and evolution

#### *3.1.1 Non-ideal MHD disc model*

In this work we have post-processed 3D non-ideal magnetohydrodynamic (MHD) simulations of protostellar disc formation presented in Zhao et al. (2018), using the code ZEUSTW (Krasnopolsky, Li & Shang 2010). They employed a spherical grid that is non-uniform along the radial axis, to provide high resolution in the inner regions of the grid. The grid boundary has a 2 au radius and a 6684 au outer radius. All gas that flows into this 2 au central cell is considered to be accreted by the protostar. No additional sink particles were included in the simulations. These simulations start from the cloud core scale and evolve up to ∼20 kyr after the formation of a rotationally supported disc, during which ambipolar diffusion plays the dominant role. We have selected the model *2.4Slw-trMRN* from table 1 in Zhao et al. (2018). This core is initialized as an isolated isothermal sphere of uniform density ($\rho_0 = 4.77 \times 10^{-19}$ g cm$^{-3}$), with core radius $R_c = 6684$ au, core mass $M_c = 1\,M_\odot$ and a constant temperature of 10 K. Assuming a mean molecular mass of $\mu = 2.36$ amu, the gas number density for molecular hydrogen correspond to $n(H_2) = 1.2 \times 10^5$ cm$^{-3}$. The core initially rotates as a solid body with angular speed $\omega_0 = 10^{-13}$ s$^{-1}$, which leads to a rotational to gravitational energy ratio of $\beta_{\rm rot} = 0.025$. The core is magnetized and the initial magnetic field is uniformly distributed, along the rotation axis, having a constant strength of $B_0 = 4.25 \times 10^{-5}$ G, which corresponds to a dimensionless mass-to-flux ratio of $\lambda = 2.4$.

The selected simulation model shows a relatively compact disc of ∼50 au in diameter, without obvious spiral structures, due to the strong magnetic field and slow rotation of the initial core. We selected the time-step at which the disc mass was the highest (0.09 $M_\odot$). The disc is only marginally gravitationally unstable (see Fig. C1) and relatively smooth, although at earlier times developing transient spiral arms. This snapshot represents a state ∼144 kyr after the beginning of the core collapse and ∼22.34 kyr after the formation of a first core (Larson 1969). Face-on and edge-on slices of the gas density and gas temperature distributions of the MHD disc model are shown in Fig. 2.

Starting from the inner boundary, the radial density distribution on the mid-plane goes as follows: the maximum is reached at the inner boundary region of 2–3 au with a density of $4.5 \times 10^{-11}$ g cm$^{-3}$ ($n_{\rm gas} = 1.14 \times 10^{13}$ cm$^{-3}$). The density remains roughly constant up to 7 au and then falls as a power law of $r^{-2.8}$ until the disc's outer edge at 25 au. The overall density distribution is rather smooth across the entire disc with no signs of fragmentation. The vertical density distribution shown in the edge-on view of Fig. 2 indicates the presence of a mid-plane much denser than the outer layers, especially within the inner 7 au and a scale height of $\lesssim 5$ au.

The initial stages of the collapse proceeded isothermally at 10 K and then followed an adiabatic equation of state (EOS; see appendix A in Zhao et al. 2018) after a density threshold of $10^{-13}$ g cm$^{-3}$ was reached. The gas temperature is then obtained from a barotropic EOS with an adiabatic index of 5/3 (up to $10^{-11}$ g cm$^{-3}$) and therefore follows always the density distribution. The edge-on view of the temperature (see lower-right panel in Fig. 2) shows a gradient from the outer layers towards the mid-plane. In this warm mid-plane, the hottest regions are at $T \sim 190$ K and lie within the densest 7 au radius.

The edge-on view of the disc also shows bipolar outflows and accreting flows from the parent dense core.

#### *3.1.2 RHD gravitationally unstable disc model*

We also model the formation of a disc in which temperature evolution is followed self-consistently along with the hydrodynamics. For



Downloaded from https://academic.oup.com/mnras/article/508/2/2583/6372913 by University of Leeds user on 28 June 2022

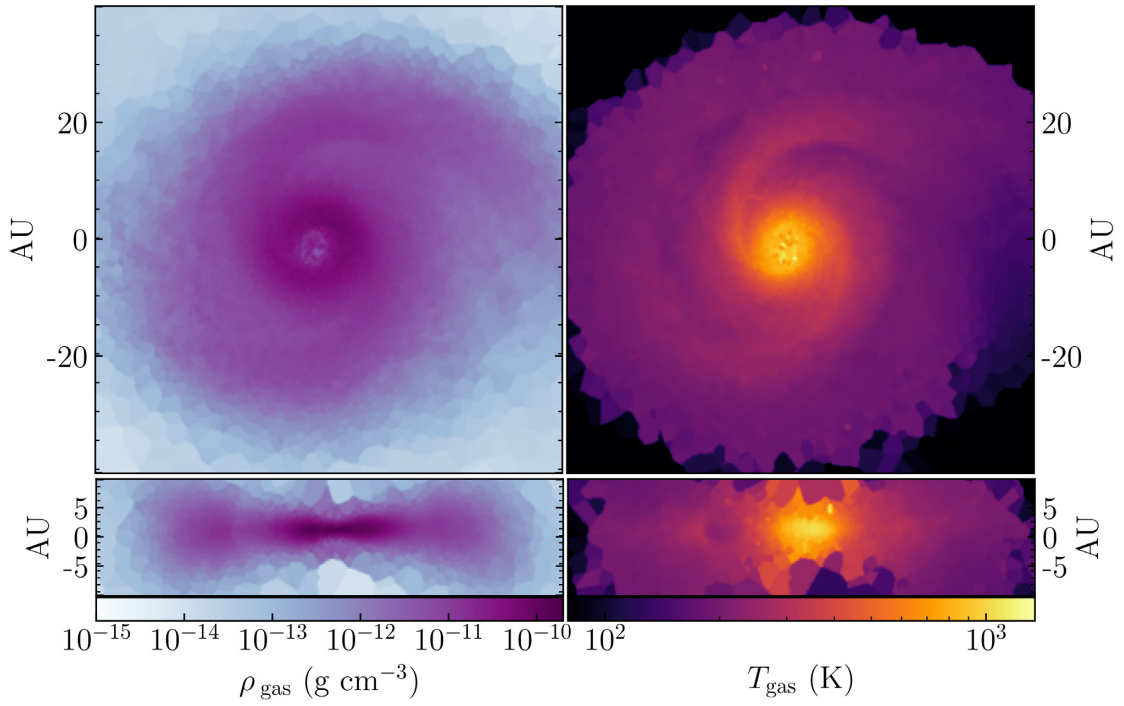


**Figure 3.** Face- and edge-on slices of the gas density (left-hand column) and gas temperature (right-hand column) distributions for the RHD the gravitationally unstable model, as described in Section 3.1.2.

this, we utilize the smoothed particle hydrodynamics (SPH) code SPHNG (Bate, Bonnell & Price 1995) including the hybrid grey radiation transfer scheme of Forgan et al. (2009) to perform radiation hydrodynamic (RHD) simulations. In this case, material is able to exchange energy via flux-limited diffusion (see e.g. Bodenheimer et al. 1990; Whitehouse & Bate 2004) and the gas is able to cool radiatively according to its local optical depth (estimated from the local gravitational potential, see Stamatellos et al. 2007). We note that this approach does not consider any magnetohydrodynamic processes.

We follow the evolution of a spherical, isothermal cloud of mass 1 $M_\odot$ and radius 2000 au using $5 \times 10^5$ SPH particles with a background temperature of 5 K. After approximately 17 kyr, a rotating disc is formed at the centre of the cloud. For the rest of this work, we consider the disc physical structure at 18.2 kyr of evolution, approximately 1000 yr after the disc first forms. At this point, the mass of the disc is 0.3 $M_\odot$ and the sink particle close to the centre of the disc has a mass of 0.2 $M_\odot$. The disc is gravitationally unstable, with a Toomre $Q$ parameter (Toomre 1964) below 1.7 (the critical value for non-axisymmetric perturbations; Durisen et al. 2007) at radii larger than 7 au and a minimum value of ∼1.4 at approximately 20 au (see Fig. C1). While the disc does not undergo fragmentation during the period of time that we simulate, it does exhibit significant non-axisymmetric structures in the form of two spiral arms within the disc. Face-on and edge-on slices of the gas density and gas temperature distributions of the RHD disc model are shown in Fig. 3.

The radial dependence of gas density is similar to that of the MHD model: it reaches a maximum value of $5 \times 10^{-11}$ g cm$^{-3}$ at around 4 au, then stays roughly constant until 7 au, where it starts to decrease as $r^{-2.6}$ until ∼40 au. Between 3 and 13 au both models have very similar density values and profiles. Beyond this region, the RHD model is denser than the MHD model by a factor of ∼2.5. Additionally, the density in the RHD disc model is not as smoothly distributed as in the MHD case, even when the two are marginally gravitationally unstable, since the spiral arms are more than twice as dense as the rest of the disc.

Since the RHD model includes a radiation transfer scheme, the temperature evolution is not only dependent on the hydrodynamics but also on the local radiation field. As a result, the coupling between the temperature and density is not as tight as in the MHD model. The disc temperature is the highest ($T \gtrsim 700$ K) within the inner ≲5 au, peaking at the very centre with values of around 1000 K. However, the temperature at the centre can be affected by artificial viscosity present in SPH simulations in regions of very high density, as those in the central few au (Bate et al. 1995; Forgan et al. 2009). For this reason, when comparing with the observations, we do not focus on the values reached in the very central region which we conservatively consider to be within 10 au. Beyond 10-15 and up to around 30 au, the overall temperature distribution follows that of the density, with temperature contrasts of 1.5–2 between the spiral arms (≲500 K) and the rest of the disc. These outer regions are much hotter (∼200 K) than the MHD disc model (∼50 K) by a factor of about 4. The adiabatic equations of state of both models are very similar, but the treatment of the heating and cooling used in this model self-consistently produces higher temperatures at radii of 10–25 au. This is possibly due to a combination of the high gas densities and kinematics processes that lead to additional compression/shock heating.

The vertical temperature structure follows a similar gradient to that of the MHD model, increasing from the outer layers to the mid-plane.

## 4 RADIATIVE TRANSFER

We have post-processed the disc models previously introduced, by performing radiative transfer (RT) calculations on their density struc-

Downloaded from https://academic.oup.com/mnras/article/508/2/2583/6372913 by University of Leeds user on 28 June 2022

tures, with the publicly available code POLARIS[1] (v4.06) (Reissl, Wolf & Brauer 2016). We use as input the density, velocity and magnetic field distributions at the time-steps of interest. We also consider the gas temperature from the simulations whose effects will be discussed below.

To facilitate the direct comparison between numerical simulations and real observations, POLARIS supports user-defined input grids, which could be converted from the snapshot of a full 3D-MHD code. In this work we have converted the models from Zhao et al. (2018; see Section 3.1.1) in spherical grid structure into the POLARIS spherical grid format and publicly released the code used for the task.[2] For the RHD model (see Section 3.1.2), the conversion was done from a non-grid-based SPH data into a POLARIS Voronoi mesh format, mapping each SPH particle into one cell.

### 4.1 Dust grain size distribution and composition

Both the generation of dust temperature fields and the ray tracing of the dust continuum emission depend strongly on the dust opacity. This wavelength-dependent opacity is determined by the composition of the dust mixture and the distribution of grain sizes. The dust component included in our set-up is a mixture of spherical silicates and graphites, meant to resemble the dust composition in the interstellar medium (Mathis, Rumpl & Nordsieck 1977) and in protostellar cores (Ossenkopf & Henning 1994). The mixture contains a 62.5 per cent (mass fraction) of silicates and a 37.5 per cent of graphites. This mixture has been commonly used in previous work using POLARIS and at similar stages of star formation (Reissl et al. 2016; Brunngräber & Wolf 2018; Valdivia et al. 2019; Brunngräber & Wolf 2020; Kuffmeier et al. 2020). As the temperatures in the disc are mainly above the sublimation temperature of interstellar ices, no ice component has been included in the dust model. The graphite component follows the 2/3–1/3 relation for cross-sections perpendicular and parallel to the incident electric field (Draine & Malhotra 1993). This means that 37.5 per cent of the graphite is split into 25 per cent and 12.5 per cent of the perpendicular and parallel components, respectively. The densities of the silicates and graphites are 3.5 and 2.2 g cm$^{-3}$, respectively, leading to a mixture density of 2.896 g cm$^{-3}$. For all radiative transfer calculations, we have assumed a gas-to-dust mass ratio of 100.

The dust opacity is calculated from the refractive indices (a.k.a., dielectric constants) using the Wolf & Voschinnikov approach (Wolf & Voshchinnikov 2004), which is in turn an implementation of the commonly used Bohren & Huffman approach (Bohren & Huffman 1983) optimized for large size parameters ($x = 2\pi a/\lambda$). We have used the refractive indices for astronomical silicates and graphites from the POLARIS repository, which are based on Draine & Lee (1984), Laor & Draine (1993), and Weingartner & Draine (2001).

POLARIS performs no mixing between the refractive indices of the two dust components (e.g. Bruggeman or Maxwell-Garnet mixing, see Ossenkopf 1991), rather it lets the two species coexist in every cell and compute the total opacity as a sum of single opacities weighted by the mass fraction (see e.g. Das, Voshchinnikov & Il'in 2010) and removes them from the cell if the dust temperature ever exceeds the sublimation temperature of the material. The sublimation temperatures of silicates and graphites are 1200 and 2100 K, respectively.

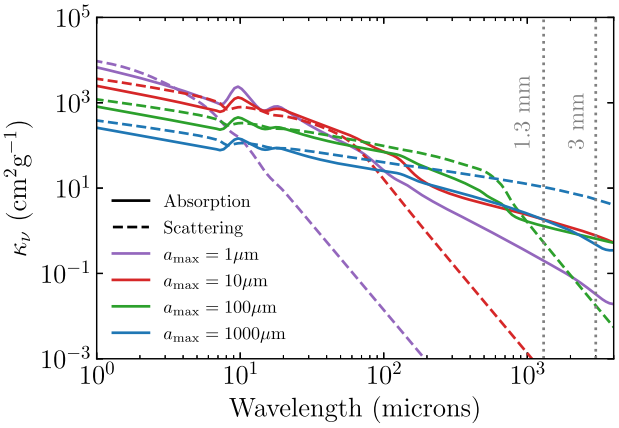


**Figure 4.** Absorption (solid lines) and scattering (dashed lines) opacities (in units of cm$^2$ per gram of dust) for dust grains of silicate plus graphite composition. All opacities were obtained assuming a grain size distribution with $q = 3.5$ and a minimum grain size of 0.1$\mu$m. Dotted vertical lines at 1.3 and 3 mm indicate the wavelengths of interest in this study.

The sizes of the dust grains follow a power-law distribution $N(a) \propto a^{-q}$, with $q = 3.5$, distributed among 200 logarithmically spaced size bins and 200 logarithmically spaced wavelengths. We chose a minimum grain size of $a_{\rm min} = 0.1$ $\mu$m, based on the value used in the disc simulations from Zhao et al. (2018) analysed here and also consistent with recent simulations of grain growth in dense cores, showing that the population of very small grains is rapidly lost as they are swept out by larger grains (Silsbee et al. 2020). This parameter was kept fixed since it has been shown that variations in the lower limit of the grain size distribution do not produce significant effects on the submillimetre and millimetre opacities (Woitke et al. 2016). The maximum grain size ($a_{\rm max}$), on the other hand, directly affects the slope of the opacity curve (known as the opacity index $\beta$) at submillimetre and millimetre wavelengths. The opacity distributions generated by this mixture are shown in Fig. 4 for different $a_{\rm max}$.

Scattering opacities are commonly assumed to be negligible at long wavelengths. This is also consistent with our results for the dust opacity as long as the $a_{\rm max} \leq 100$ $\mu$m. In this work we have assumed $a_{\rm max} = 10$ $\mu$m. This results in the flux from the discs being mainly produced by thermal emission.

Since the focus of this study is not to constrain the grain sizes but to test if any of the presented numerical models can be a good fit to the new high-resolution observations of source B, we did not explore all the parameter space for $a_{\rm max}$, which would be analysed in a future work. Considering that there is no unambiguous evidence of large grains at the early Class 0 protostellar stage, as a first step we consider only grains with $a_{\rm max} \leq 10$ $\mu$m. This choice also results in most of the continuum emission coming from thermal dust emission, since the opacity of scattering is very low compared to that of absorption. The dominance of absorption opacities in the millimetre wavelengths is relevant for understanding the flux distributions; however, for the calculation of temperature distributions, the full extinction opacity (scattering plus absorption) at all wavelengths was used.

Finally, the extinction dust opacities used in this study are $\kappa_{\rm ext}^{1.3\ {\rm mm}} = 1.50\,{\rm cm^2\,g^{-1}}$ and $\kappa_{\rm ext}^{3\ {\rm mm}} = 0.58\,{\rm cm^2\,g^{-1}}$, as shown in Fig. 4.

[1] http://www1.astrophysik.uni-kiel.de/~polaris
[2] https://github.com/jzamponi/zeus2polaris



Downloaded from https://academic.oup.com/mnras/article/508/2/2583/6372913 by University of Leeds user on 28 June 2022

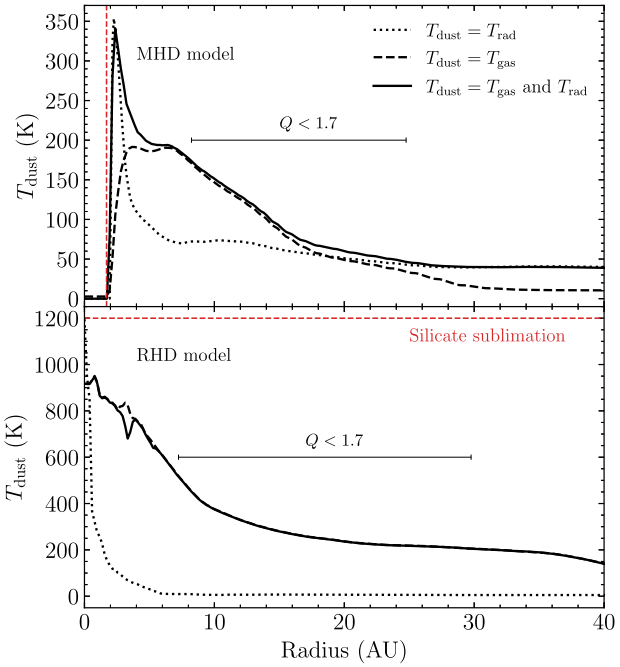


**Figure 5.** Radially averaged mid-plane dust temperatures. Temperatures are shown for the MHD disc formation model (top panel) and for the RHD gravitationally unstable disc (bottom panel). In both panels, the dotted line represents the dust temperature produced by radiative heating from the central source only, the dashed line represents the temperature assuming $T_{dust} = T_{gas}$, and the solid line represents a combination of both effects, as described in Section 4.2.2. The red dashed line in the upper panel placed at 2 au represents the inner boundary in the MHD model, and the red line in the lower panel represents an upper limit for the dust temperature set by the sublimation of silicates. The region where $Q$ <1.7 represents the extensions over which the disc is considered to be gravitationally unstable, as described in Appendix C.

### 4.2 Dust temperature distributions

#### *4.2.1 Dust temperatures from stellar radiation*

We have generated 3D distributions of the dust temperature for both disc models, by heating the dust with the radiation from a central star. We first consider the dust temperature generated only from stellar radiation, with no inclusion of the gas temperature from the numerical simulations (shown in Figs 2 and 3). For this, we placed a point source in the centre of the grid, radiating as a blackbody (i.e. a protostar) with $R_{star} = 3\ R_{\odot}$ and effective temperature $T_{eff} =$ 4000 K. This results in a luminosity of $L_{star} = 2.1\ L_{\odot}$, split among $10^8$ photons ($N_{ph}$). These stellar parameters are similar to the findings obtained by Jacobsen et al. (2018) using radiative transfer modelling of both protostellar sources (A and B) in IRAS16293−2422. They constrained the individual luminosities to $L_A = 18\ L_{\odot}$ and $L_B \leq 3\ L_{\odot}$ for A and B, respectively.

Fig. 5 shows the radially averaged mid-plane dust temperatures for both disc models. The temperature generated by star heating is only relevant within the very central zones in both cases, because the densities in the discs shield the outer regions from stellar radiation. In the MHD case, radiative heating overcomes the gas heating only up to 2 au outside the inner boundary and falls below ∼60 K at larger radii. In the RHD case, it slightly overcomes the gas temperature at sub-au scales and then rapidly falls to a few K at 6 au, showing no contribution to the overall temperature field. We have also tested whether these results are dependent or not on the value of the opacities used and found that they hold (i.e. the disc does not heat up significantly beyond a radius of 10 au) even when increasing or decreasing the opacity by an order of magnitude. More details on such tests are described in section 6.3.

#### *4.2.2 Dust temperatures combining stellar radiation and MHD/RHD gas temperatures*

In this section, we consider both the gas temperature obtained from the heating mechanisms present in the MHD and RHD simulations $T_{gas}$ (see Section 3), and also the dust temperature provided by radiative dust heating $T_{rad}$. POLARIS allows to combine these two temperatures in order to account for heating at all scales. We provide here a brief explanation of the combination process and refer the reader to Reissl et al. (2016) for further details. In the case of a model with non-zero initial temperature, as for instance, when providing the temperature from the gas, the energy of a cell is considered to be the sum of the energy produced by radiation and that associated to the gas temperature. To obtain the energy of the gas temperature, POLARIS compares the new cell energy to the emissivity produced by the gas temperature and solve for the energy offset. Once the energy information is updated, the dust temperature is recalculated accordingly.

The gas temperatures in the MHD simulations are given by the EOS while in the RHD simulation the gas is able to cool radiatively according to its local optical depth (Stamatellos et al. 2007) and exchange energy via flux-limited diffusion (Bodenheimer et al. 1990; Whitehouse & Bate 2004). The radially averaged profiles for the $T_{dust} = T_{gas}$ and $T_{rad}$, as well as for the $T_{dust} = T_{gas}$ only case for both disc models are shown in Fig. 5.

From this figure, we conclude that for the MHD model, radiation from the protostar dominates within the first 4 au, but beyond that radius the temperature from the EOS dominates up to around 18 au. At larger radii ($\gtrsim$20 au) outside disc edge, the protostellar heating dominates again resulting in a fairly constant temperature of 40 K. On the other hand, for the RHD model the protostar radiation is not able to penetrate beyond 1 au due to the high optical depth. Therefore, the disc temperatures at the scales where the spiral arms are located are not dominated by protostellar heating. Instead, the high dust temperature here is a result of the high gas temperature, which is also higher than the one reached by the MHD model. The resultant high dust temperature is due to the efficient thermal coupling at high densities. It is non-trivial to disentangle the sources of extra heating in the RHD model versus the MHD model because they can come from different sources. For instance, the models were generated with a different numerical set-up, i.e. SPH versus grid-based code, with and without magnetic fields or radiative transfer and slightly different initial conditions. As pointed out by Whitehouse & Bate (2006) the thermal evolution of different set-ups is expected to be different. Moreover, they also discuss that the use of an EOS can underestimate the temperature of the gas surrounding the central highest density. This was also recently demonstrated specifically for the case of a gravitationally unstable disc (Xu & Kunz 2021b). In addition, the spiral arms do add extra compression heating, responsible for the local temperature rise.

While a comparative modelling study to investigate this is beyond the scope of this work, we can still rule out some possible reasons for the different temperature. For instance, it is not due to the RHD having higher density than the MHD model since the models show different temperatures while covering a similar density range. Likewise, the thermal evolution of the central density of the RHD code (shown in fig. 8 of Forgan et al. 2009) and of the MHD code

Downloaded from https://academic.oup.com/mnras/article/508/2/2583/6372913 by University of Leeds user on 28 June 2022

(see fig. A1 from Zhao et al. 2018) is comparable. Also it is not due to the RHD disc being more optically thick, as a set-up fully based on an EOS (with no cooling) would represent an optically thick limit.

Based on this analysis, we conclude that an extra source of heating is needed to explain the high brightness temperatures observed and that gravitational instabilities in the disc provide a relatively simple explanation for it. As discussed in Xu & Kunz (2021b), the lower the Toomre $Q$ parameter, the larger the accretion rates which naturally result in higher temperatures.

### 4.3 ALMA synthetic observations

The ideal intensity distributions produced by POLARIS, in units of Jy pixel$^{-1}$, needed to be post-processed assuming a certain observing set-up and telescope, in order to properly compare them with real observations. Because our goal is to compare our results to ALMA observations, we performed the synthetic observations using CASA, which provides the right tools to simulate ALMA observations. We first adjusted the header of our images to match those from the data at 1.3 and 3 mm described in Section 2.1. We then used the `SIMOBSERVE` task to generate the complex visibilities and finally cleaned the images using the `TCLEAN` task. The observing and imaging set-ups for each frequency are slightly different since the real data was observed in different occasions and with different set-ups

Visibilities were first generated at the frequency of 223 GHz (1.3 mm; band 6), with a bandwidth of 0.12 GHz towards the sky coordinates 16 h 32 m 22.63 s −24 d 28 m 31.8 s and using the array configuration C43-7 from Cycle 4. Such a set-up achieves a synthesized beam of 0.082 arcsec × 0.067 arcsec. The total observing time was 1.25 hours. Images were cleaned in multifrequency synthesis (`mfs`) mode, with a `STANDARD` gridder and a `MULTISCALE` deconvolver. The visibilities were cleaned interactively using a `BRIGGS` weighting scheme with a robust parameter of 0. For the observations at 1.3 mm only, we narrowed the range of baselines (*uv*-range) from 120 to 2670 kλ. The 3 mm observations shared the same set-up, except that they were centred at the frequency of 99.99 GHz (band 3) with a bandwidth of 2 GHz using the most compact array configuration C43-10 from Cycle 5. Such a set-up achieves a synthesized beam of 0.042 arcsec × 0.039 arcsec. Since the resolutions of the simulated observations are slightly higher than those of the real ALMA observations, all synthetic maps have been smoothed to match the respective resolution of the real observations.

## 5 COMPARISON WITH OBSERVATIONS

### 5.1 Brightness profiles

Based on the intensity distributions generated by the radiative transfer calculations, we performed synthetic ALMA observations using the two disc models described in Section 3 as sources. The observations were simulated with CASA (v5.6.2) following the procedure previously described in Section 4.3. We analysed the resulting images by generating cuts of the temperature brightness along the horizontal (east–west) axis and studied their similarities to the brightness profile from the real observations presented in Section 2.2. The resulting profiles are shown in Fig. 6 at 1.3 (left-hand column) and 3 mm (right-hand column) for the MHD (upper panels) and RHD (lower panels) disc models. Profiles are shown for the real observation (semi-dotted black) and for different disc inclinations from 0 (face-on) to 40° (rotated around the north–south direction) and assuming the opacity generated by a size distribution with $a_{\rm max} = 10\,\mu$m. The brightness temperatures are presented as a function of angular offset with respect to the peak emission, i.e. the zero offset corresponds to the peak in each image.

We have also tested the effects of a dust opacity with $a_{\rm max} = 1\,\mu$m (i.e. $\kappa^{1.3{\rm mm}} = 0.29$ cm$^2$ g$^{-1}$ and $\kappa^{3{\rm mm}} = 0.05$ cm$^2$ g$^{-1}$), which is closer to ISM values (Mathis et al. 1977). However, the simulated emission with $a_{\rm max} = 1\,\mu$m fails to reproduce the observed 3 mm fluxes at scales of ∼20 au from the peak, by a factor of ∼80 for the MHD model and ∼5 for the RHD model. With this smaller $a_{\rm max}$, not only the fluxes are underestimated but also the disc looks much smaller and is incapable of reproducing brightness asymmetries with any of the two models. For this reason, the results presented hereafter, are all obtained assuming $a_{\rm max} = 10\,\mu$m.

Based on the analysis presented in Section 4.2 and shown in Fig. 5, for our set-up, the heating provided by protostellar radiation is only important when the gas temperature in the disc is relatively low ($T \sim 150$ K), as it is in the case of the MHD model. Therefore we consider both sources of heating (i.e. $T_{\rm dust} = T_{\rm gas} + T_{\rm rad}$) when producing the synthetic emission maps of the MHD model. As the MHD model has a central hole (the inner boundary) with no temperature or density, we filled this hole before the ALMA simulations with a constant flux equal to the average values in the innermost ring (optically thick approximation). We note, however, that the angular extent of this hole is only 0.03 arcseconds and does not contribute significantly to the peak flux.

In the RHD model, the compression/shock heating overcomes radiative heating at almost all radii, and therefore, the results shown for the RHD model considered the dust temperature as provided by the gas temperature only ($T_{\rm dust} = T_{\rm gas}$). Regardless, the inclusion of the protostellar heating in this model would only change the fluxes of the peak, which we are not analysing since the gas temperatures in this region can be overestimated due to the effect of the artificial viscosity (as explained in Section 3.1.2).

Fig. 6 shows that the peak brightness generated by the MHD model underestimates the values observed with ALMA by factors of 1.7 and 2, at 1.3 and 3 mm, respectively, when the disc is observed face-on.

We have also tested the effect of increasing the luminosity of the central protostar to 5 and 20 L$_\odot$, but this is still underestimating the fluxes even in the most luminous case, in agreement with the above-mentioned finding of rapid shielding from stellar flux at smaller radii. From all this parameter study, we conclude that the temperatures in the MHD disc are not capable of reproducing fluxes as high as those observed towards source B in these high-resolution observations, even when combining the temperature from both heating sources.

When considering both models beyond 10 au up to 40 au, the fluxes of the RHD model are much closer to the observed values than the case for the MHD disc. This is indeed the spatial scale at which the Toomre parameter is below 1.7 and the spiral arms are found in the RHD model. The fraction of underestimation from the MHD model at these scales (measured at a left-hand side of the peak) is around 3 and 3.5 at 1.3 and 3 mm, respectively, while for the RHD model, the corresponding overestimation fractions are only 1.4 and 1.1 (measured at 0.14 arcsec or ∼20 au). As it can be seen, the match between simulated and real fluxes is better at the higher resolution observations, namely at 3 mm.

Our results also indicate the presence of asymmetric horizontal brightness profiles in the RHD disc model, similar to what is observed in Fig. 1, and follow a similar behaviour to the left and right of



Downloaded from https://academic.oup.com/mnras/article/508/2/2583/6372913 by University of Leeds user on 28 June 2022

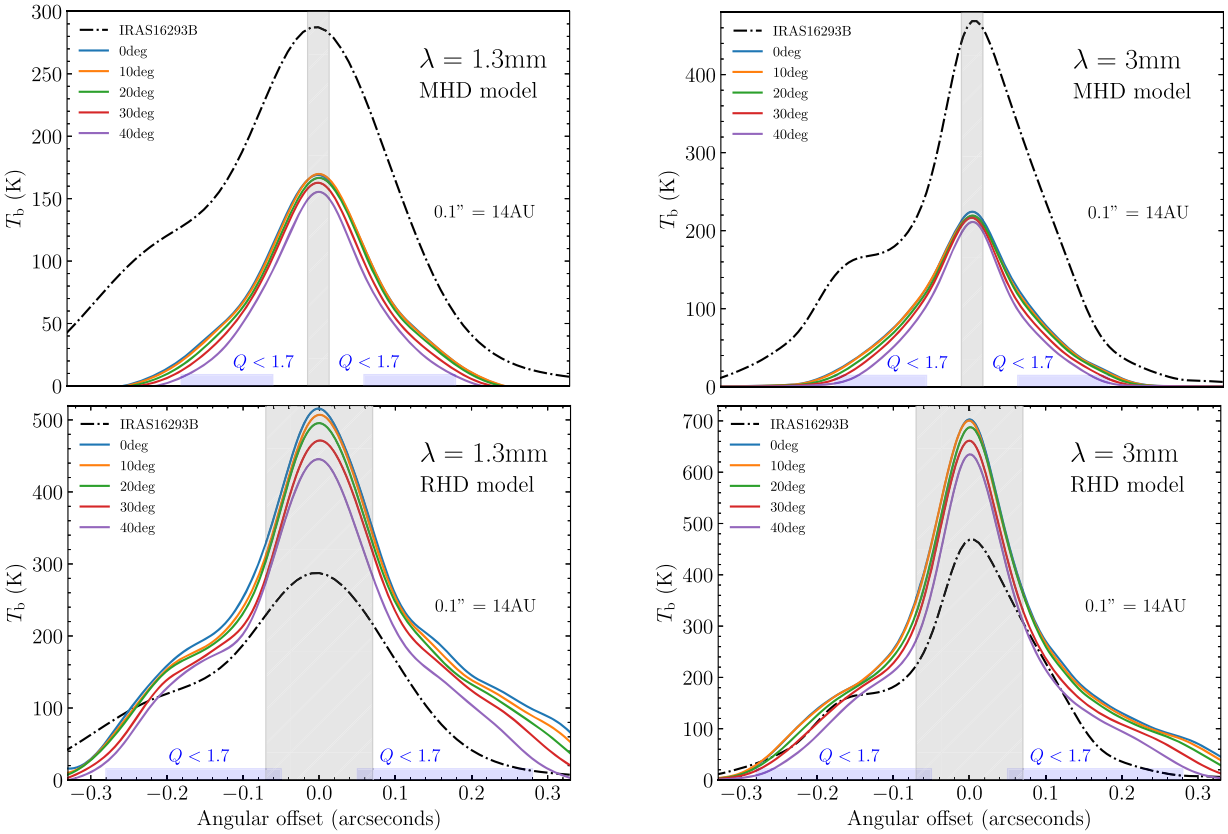


**Figure 6.** Horizontal cuts of brightness temperature distributions along the east–west direction and through the position of the peak flux. Top panels show the results at 1.3 and 3 mm, for the MHD model with $T_{\rm dust} = T_{\rm gas}$ and radiative heating. Lower panels show analogous results for the RHD model, where the disc temperature ($T_{\rm dust} = T_{\rm gas}$) is significantly higher and closer to the observed values. The grey shaded area in the MHD model represents the inner boundary of 2 au. The grey shaded region in the RHD model represents the inner 10 au in which the temperatures and therefore the fluxes can be overestimated by numerical high viscosity. The blue shaded region in all panels indicates the extensions over which the disc is considered to be gravitationally unstable, as described in Appendix C. The angular offset is measured with respect to the peak emission in each image.

the peak, i.e. a rapid decrease in intensity until 0.1 arcsec offset (14 au; $T_{\rm b} \sim 180$ K) followed by a constant drop on the right and a two-phase drop (a.k.a, wing) on the left. Both features are best matched at the highest resolution observations taken at 3 mm. The asymmetric feature of the observations lies within offsets $\sim -0.07$ and $-0.3$ arcsec. These are exactly the spatial scales at which the spiral arms are found in the RHD disc model ($\sim$10-40 au; see Fig. 3), which supports that this type of asymmetry could be produced by the presence of spiral arms. However, this is only one possibility for the origin of the asymmetry and we acknowledge that other processes such as asymmetric accretion from the envelope on to the disc, based on the detection of infalling material (Pineda et al. 2012), may also be taking place. Further parameter space explorations are needed to rule-out any of the possible scenarios.

We also find that the more inclined discs produce lower fluxes than the face-on case. This can be explained by the higher optical depth obtained when the line of sight (LOS) goes through more disc material, as it is the case for an inclined disc.

Since the RHD model, over scales of 10 to 40 au, appears to reproduce well the observed fluxes, we conclude that the high disc temperatures reached by the RHD gravitationally unstable model represent a good match to the ALMA observations of IRAS16293−2422 B. This suggests that the gas dynamics within the disc likely play a significant role in heating the disc.

### 5.2 Synthetic maps and spectral index of the RHD gravitationally unstable model

In this section, we present the synthetic observations at 1.3 and 3 mm along with its spectral index, for the best match to our observations, i.e. the RHD model. These results are shown in Fig. 7. We also provide the results for the MHD disc model in Appendix B. Similar to the real observations, the 3 mm map has been smoothed with the beam of the 1.3 mm observation before computing the spectral index. We present the results obtained by a dust grain size distribution with $a_{\rm max} = 10$ μm and for the face-on projection. At both wavelengths, the peak is approximately centred, although the extended structure is not circular or entirely symmetric. The substructures present in the disc, such as spiral arms (see Fig. 3) are not clearly seen at 1.3 mm (0.11 arcsec × 0.07 arcsec resolution), similar to the case with the real ALMA observations. On the other hand, the 3 mm observations, with their higher angular resolution and lower optical depth, display better the presence of spiral arms.

In analogy to Fig. 1, we present the derived spectral index between 1.3 and 3 mm (223 and 100 GHz) for the same disc model, with contours ranging from 3, 2 to 1.7. Our results indicate a drop to around $\alpha \lesssim 1.8$ at the very centre of the source, similar to what is observed in the ALMA observations (see Fig. 1). This result is not only found in the case of the RHD disc model. In Fig. B1, we show

Downloaded from https://academic.oup.com/mnras/article/508/2/2583/6372913 by University of Leeds user on 28 June 2022

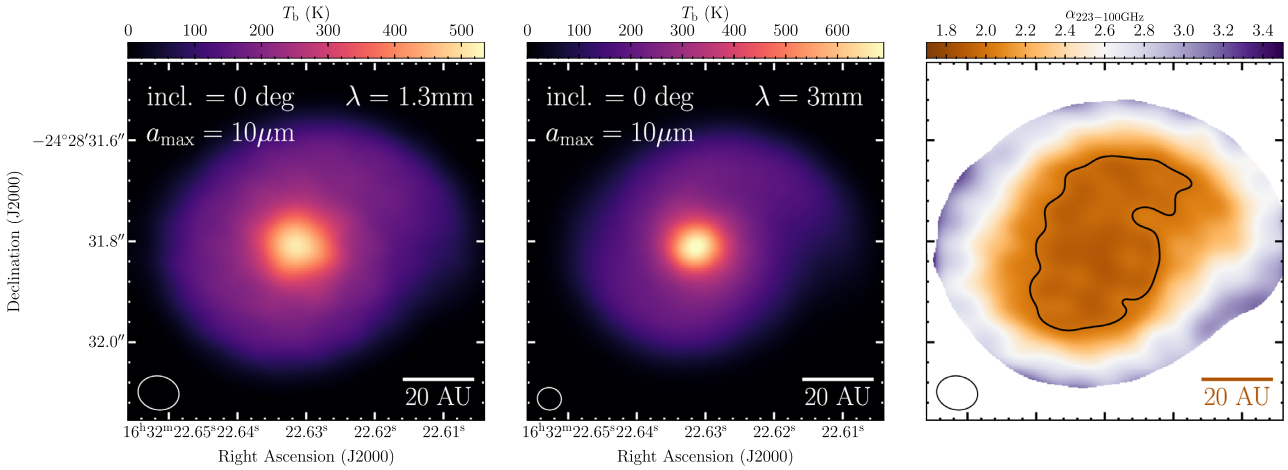


**Figure 7.** Synthetic brightness temperature maps at 1.3 and 3 mm along with the spectral index for the gravitationally unstable RHD model. The spectral index map reproduces well the trends seen in the observed map shown in Fig. 1. The contour for the spectral index indicates the $\alpha = 2$ region.

the results for the MHD disc model in a similar layout as Figs 1 and 7. The spectral index found in the MHD case is consistent with both the ALMA observations and the RHD model, with a tendency to decrease towards the centre, reaching values as low as 1.7. In Section 6.1 we discuss the origin of such a low $\alpha$ values in the observations and both models.

## 6 DISCUSSION

### 6.1 Are early discs hotter towards the mid-plane?

The tendency for the spectral index $\alpha$ to decrease at the centre of the discs found in the ALMA real and synthetic observations is an interesting observational feature that can provide us with information about the internal structure of early discs. The spectral index not only provides information on the slope of the SED but also indicates the presence of temperature gradients along the LOS. The dust opacity for a given grain size distribution follows a power-law function of wavelength and is therefore higher at 1.3 than at 3 mm. If the disc becomes optically thick along the LOS at both wavelengths, each wavelength will trace a different temperature layer within the disc, with the longer wavelength tracing the more deeply embedded layer. In the case of a positive temperature gradient towards the denser inner regions, which is the opposite of what is expected for more evolved passive discs (see e.g. Kenyon & Hartmann 1987; Chiang & Goldreich 1997; Dartois, Dutrey & Guilloteau 2003; Dullemond et al. 2007; Armitage 2009, 2011; Kama, Min & Dominik 2009; Lizano et al. 2016; Tapia & Lizano 2017; Paneque-Carreño et al. 2021) where the dust temperature is mainly determined by radiative heating, lower frequency observations will trace hotter layers than higher frequency observations, leading to $\alpha \lesssim 2$ values as described in Appendix A.

In principle, the brightness temperature resulting from our synthetic observations should trace the dust temperature of the layer within the disc at which the optical depth $\tau$ becomes unity (see also Evans et al. 2017). To prove our point, we show in Fig. 8 the 2D dust temperature distribution of the RHD disc at the $\tau = 1$ surface for both wavelengths, convolved with the corresponding beams of the ALMA observations. Such temperature structures match well those obtained from the radiative transfer calculations indicating that indeed both wavelengths trace two different temperature distributions or layers from different depths within the disc.

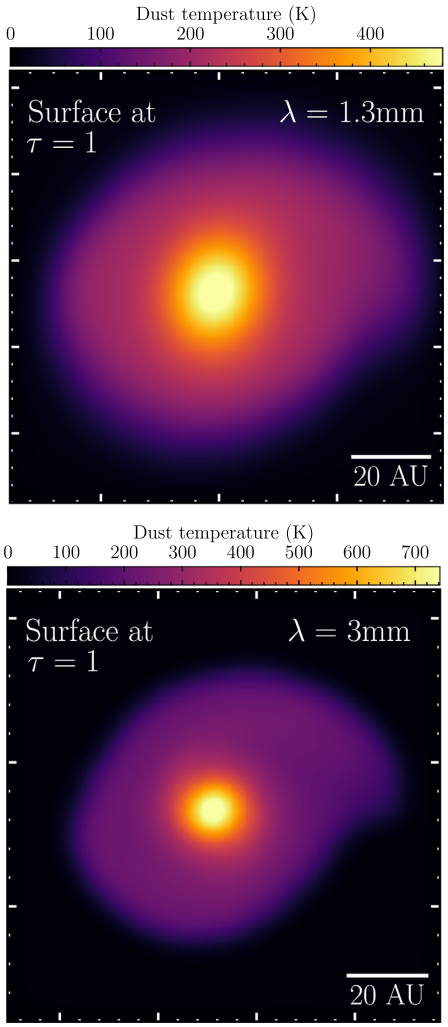


**Figure 8.** 2D face-on distribution of the dust temperature ($T_{dust} = T_{gas}$) from the RHD gravitationally unstable model, at the surface where the optical depth becomes unity. The temperature matches well the brightness temperature distributions shown in Fig. 7, demonstrating that the two wavelengths are indeed tracing different layers. A 3D view of such surfaces is shown in Fig. 9.



Downloaded from https://academic.oup.com/mnras/article/508/2/2583/6372913 by University of Leeds user on 28 June 2022

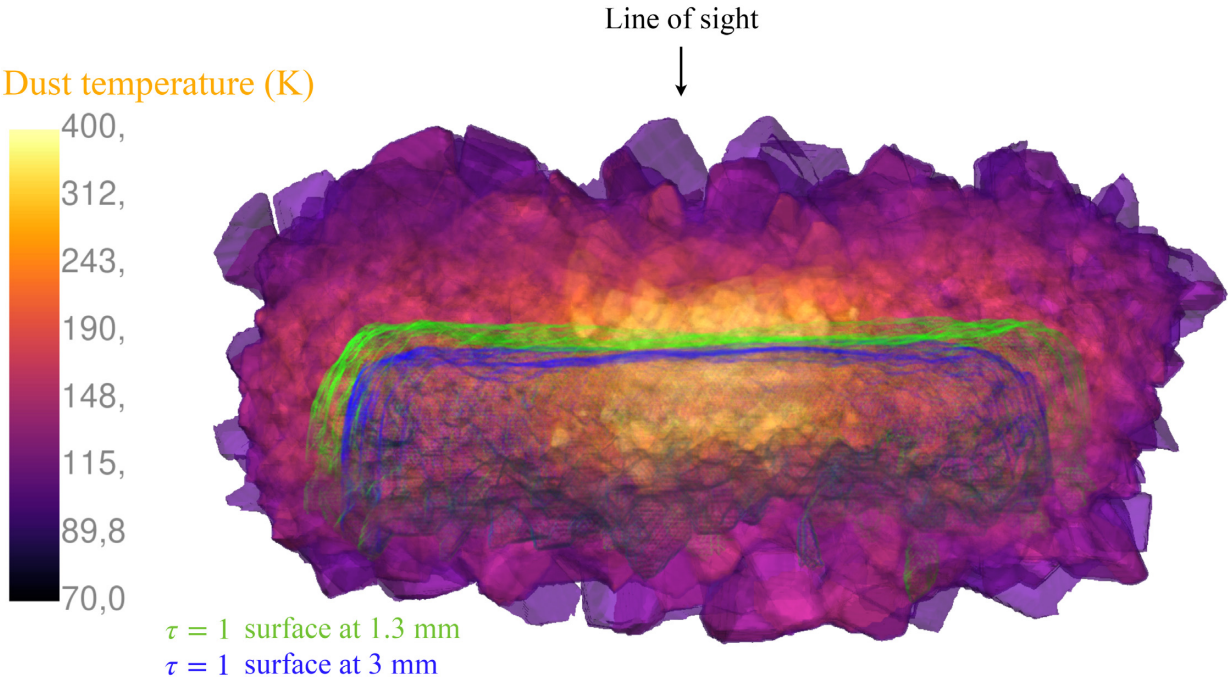


**Figure 9.** 3D rendering of the dust temperature ($T_{\rm dust} = T_{\rm gas}$) for the RHD disc model in edge-on projection. The green and blue surfaces represent the $\tau = 1$ layers at 1.3 and 3 mm, respectively. From the observer's point of view, the two optically thick surfaces lie at different depths within the disc and therefore trace dust layers at two distinct temperatures.

In Fig. 9 we present a 3D rendering of the dust temperature field of the RHD model, represented by the black-to-yellow coloured isocontours and we include the $\tau = 1$ surfaces at 1.3 and 3 mm in green and blue, respectively. Assuming the observer is placed far above the top surface of the disc, this illustration shows the regions of the disc that the observations at 1.3 and 3 mm have access to. We obtain a similar result for the MHD model, which fluxes although too low for reproducing source B observations, can match observations towards other less luminous Class 0 discs. Hence, our results from these two models indicate that positive temperature gradients towards the inner denser regions in gravitationally unstable discs can naturally explain the observations of low spectral index towards young disc sources, especially those with values below 2. These low spectral indices are usually interpreted as a sign of early grain growth, but early discs being warmer in their interior as compared with the later Class II discs is an alternative scenario, one that better matches with the theoretical predictions showed in this work. This scenario has also been suggested in previous works in which analytical temperature and density profiles were assumed (Galván-Madrid et al. 2018; Lin et al. 2021).

Recent constraints from molecular line observations have also shown that embedded discs are warmer than more evolved protoplanetary discs. For instance, the $^{13}$CO and C$^{18}$O observations towards the nearly edge-on disc (85°; Ohashi et al. 1997; Tobin et al. 2008; Oya et al. 2015) around the Class 0 protostar L1527, suggests that the mid-plane temperature is at least $\gtrsim$25 K (van 't Hoff et al. 2018), which is contrary to the case of CO depletion in the mid-plane of Class II discs (Guilloteau et al. 2016; Dutrey et al. 2017). Warm discs have also been observed in several other discs in Taurus (van't Hoff et al. 2020b).

The presence of a positive temperature gradient at small radii seems to be also the case in the evolved and gravitationally unstable (Dong et al. 2016) FU Ori disc (Lizano et al. 2016; Liu et al. 2019; Labdon et al. 2021). The high-resolution (0.1–10 au) observations reported by Liu et al. (2019) show the inner parts of the disc in FU Ori with temperatures above 700 K at radii $\lesssim$ 3 au. Their interpretation of the results suggests that the temperature in the inner 10 au is determined by the heating from gas kinematics and that radiative heating becomes important at larger radii; however, they acknowledge not having considered extra sources of heating (e.g. shocks and adiabatic compression) which could also dominate the viscosity as the main heating mechanism.

### 6.2 Are self-gravitating discs at the origin of some hot corinos?

The high temperatures (>100 K) of the IRAS 16293−2422 B disc implies that most of the volatile material in the dust icy mantles is thermally evaporated, including water and complex organic molecules accumulated during the pre-stellar phase. This process is likely at the origin of the rich chemistry observed by recent spectral line surveys (e.g. Jørgensen et al. 2018). It is then tempting to suggest that self-gravitating discs provide the conditions for the detections of the so-called 'hot corinos', hot regions nearby Class 0 sources, rich in complex organic molecules (e.g. Cazaux et al. 2003), since it has been shown that gravitational instabilities in a disc directly affects their chemical evolution (Ilee et al. 2011; Evans et al. 2015; Quénard et al. 2018). It is interesting to note that a self-gravitating disc with spiral arms has also been suggested to be present in the Class 0 hot corino HH 212 (Tobin et al. 2020; Lee et al. 2021; Lin et al. 2021). Additionally, another potentially gravitationally unstable disc in Orion A, HOPS-87 (Tobin et al. 2020) has been recently detected in methanol emission (Hsu et al. 2020), providing additional evidence for the presence of self-gravitating discs in hot corino sources. Studies similar to those presented here

Downloaded from https://academic.oup.com/mnras/article/508/2/2583/6372913 by University of Leeds user on 28 June 2022

should be carried out in the currently known hot corinos to test our suggestion.

We finally note that within the central 20 au, in particular along the spiral arms of the self-gravitating disc where shocks are present (see Fig. 5), the temperature can exceed 300 K (as also found by Boley & Durisen 2008), allowing efficient sublimation of carbonaceous grains (e.g. van't Hoff et al. 2020a). This is expected to affect the dust properties (as the important carbonaceous component will be locally depleted) as well as the gas phase chemical composition, due to the local increase of carbon atoms and hydrocarbons. This prediction could be tested with high angular resolution multiwavelength observations of the dust continuum emission (to measure possible opacity changes) as well as of C-bearing species (to measure possible increase of the C/O ratio at these locations) at low frequencies (to avoid dust opacity problems; e.g. De Simone et al. 2020).

### 6.3 Radiative heating under different assumptions

The complexity of a full 3D HD simulation requires that the inclusion of radiation transport should be somehow simplified as compared to a full 3D radiative transfer calculation like those performed with POLARIS. In particular, these two radiative transfer schemes differ in the frequency dependency of the opacities (Boley et al. 2006). The post-processing done in this paper is performed considering wavelength-dependent stellar fluxes and dust opacities. On the other hand, the RHD simulation makes use of a frequency-averaged opacity, the so-called Rosseland mean opacity, which changes to account for different temperature and density conditions (see fig. 3 from Forgan et al. 2009).

In Section 4.2 we discuss about the main heating mechanism determining the overall disc temperature in our MHD and RHD models. The results from the radiative equilibrium calculations suggest that protostellar radiation is not able to raise the disc temperature significantly beyond $\sim$1 au and therefore the disc temperature is dominated by dynamical processes. However, here we want to check if these results also hold when assuming different opacities. In particular, constant opacities as those used in the RHD model. In order to test this effect, we ran radiative equilibrium calculations using roughly constant opacities between 0.5 to 800 $\mathrm{cm^2\,g^{-1}}$, which covers the opacities range used in the RHD model (Forgan et al. 2009), for temperatures less than $10^3$ K. From these tests, we concluded that still protostellar heating alone is not sufficient to heat the disc to temperatures that can explain the observations. In addition, we performed these tests together with increasing the luminosity of the central source up to 20 $\mathrm{L_\odot}$ for the MHD disc, which is the less dense within the inner 5 au among the two models. We found that the temperature obtained from radiative heating alone, peaks at $\sim$400 K within 1 au and falls rapidly to 150 K at 5 au, beyond which the profile closely follows that of the gas temperature (dashed curve from the upper panel in Fig. 5). This is obtained when using 20 $\mathrm{L_\odot}$ and 80 $\mathrm{cm^2\,g^{-1}}$. This luminosity is close to the luminosity values inferred for the entire triple system IRAS 16293, and thus, represents an upper limit. As discussed in Section 5.1, this temperature profile cannot explain the observations. Therefore, heating mechanisms due to dynamical processes are needed to explain the observations.

### 6.4 Comparison to spectral index in more evolved gravitationally unstable discs

Recently, the disc mass and millimetric spectral index for the Class II gravitationally unstable disc Elias 2-27 have been reported by Paneque-Carreño et al. (2021) and Veronesi et al. (2021). This protoplanetary disc shows spiral arms on $\gtrsim$200 au scales, at which location the brightness temperature at 0.89, 1.3 and 3 mm is below 10 K, one order of magnitude lower than the observations of the Class 0 disc in this work. The derived disc mass is about 0.1 $\mathrm{M_\odot}$, this is factor of 3 lower than the RHD disc model presented in this work. The spectral index calculated using ALMA observations for Elias 2-27 at 0.89, 1.3 and 3 mm falls below 2.0 within $\lesssim$50 au radius. As they also pointed out by the authors, such a low spectral index could be due to dust scattering effects (Liu 2019), but also due to relatively low dust temperature (Sierra & Lizano 2020). Alternatively, the heating mechanisms and the radiative transfer effects introduced in our present work may also partly contribute to that result as the inner region is expected to have higher densities. Given that Elias 2-27 is consistent with being gravitationally unstable, the gas kinematics may also play a non-negligible (e.g. as compared with protostellar irradiation) role heating the inner $\sim$50 au of the disc, in particular, in the presence of spiral arms (cf., Dong et al. 2016). As a demonstration, Fig. 10 shows the synthesized spectral index maps of our RHD model at the ordinary spatial resolution. It appears that the spectral indices can be low over a relatively spatially extended area, and are particularly low at the locations of the spiral arms. How important is this effect in Elias 2-27 can be discerned by constraining the dust brightness temperature and dust temperature with future high angular resolution and multifrequency observations (e.g. including measurements at $\sim$500 and $\sim$700 GHz). The mechanisms we mentioned are not mutually exclusive. However, in the case that the low spectral indices are mainly due to low dust temperatures, the 0.89–1.3 mm spectral indices should be positively correlated with dust temperature and may not have a specific relation with the spiral structures. In the case that it is mainly due to non-radiative heating (e.g. compression or shocks), the 0.89–1.3 mm spectral index is expected to be anticorrelated with the dust temperature, and we should expect the spiral arms to be the local minimum of the 0.89–1.3 mm spectral indices.

### 6.5 The origin of the observed asymmetry

As discussed in Section 2.2.1, there is evidence also from continuum observations at $\sim$33–43 GHz, molecular line distribution and kinematics showing that the asymmetry might be real and not a product of optical depth in a highly inclined disc (Rodríguez et al. 2005; Pineda et al. 2012; Zapata et al. 2013; Oya et al. 2018; Hernández-Gómez et al. 2019a).

Spiral arms are a natural feature in gravitationally unstable discs (Kratter & Lodato 2016). Depending on the physical conditions, they can be either symmetric or highly asymmetric structures. Regardless of their shape, a disc containing spiral arms will show brightness profiles that depart from a symmetric Gaussian profile, as the ones observed in Fig. 6. The exact shape of such a brightness profile depends strongly on the shape and position of the arms. Even if the arms are symmetric, they will not necessarily produce a flux pattern with symmetric wings around the peak, as we showed in the case of the RHD model in Fig. 6. Moreover, the position of the peak in a gravitationally unstable disc must not necessarily be centred within the disc. This shift of the peak from the centre can arise by considering highly asymmetric spiral arms, unlike those shown by our RHD model. For instance, recent non-ideal MHD simulations presented by Coutens, Commerçon & Wakelam (2020) showed a spiral arm pattern, produced by considering the collapse of a non-rotating 1 $\mathrm{M_\odot}$ core initialized with turbulence. Such an asymmetric structure, likely produced by the effect of the initial turbulent velocity field and magnetic field could explain the shift of the peak observed



Downloaded from https://academic.oup.com/mnras/article/508/2/2583/6372913 by University of Leeds user on 28 June 2022

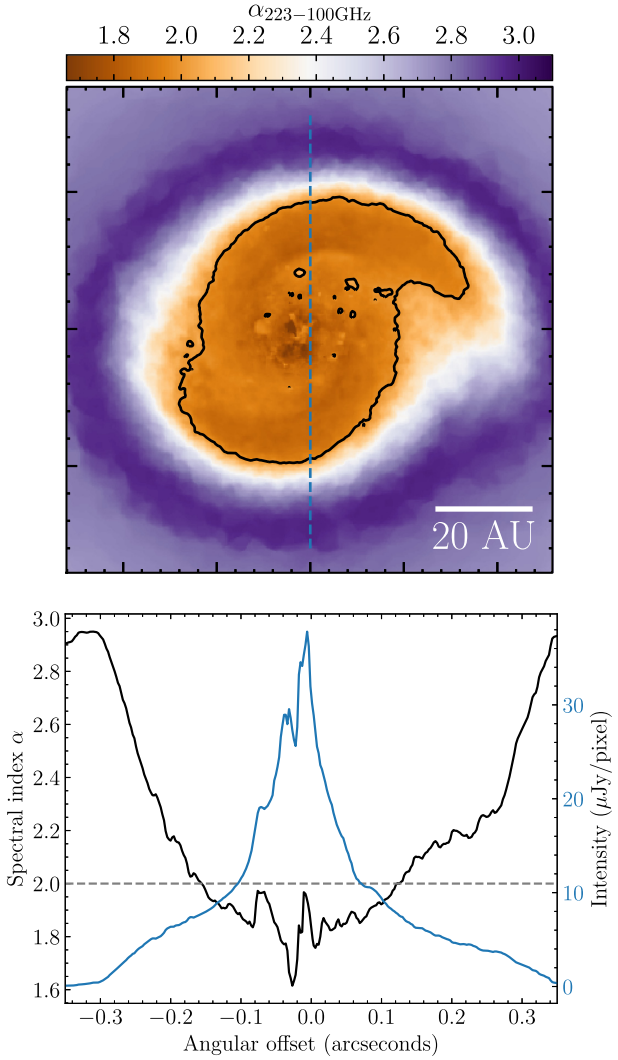


**Figure 10.** Top panel: spectral index map for the RHD model disc shown in Fig. 7 before performing the ALMA simulation, i.e. at full spatial resolution. The black contour indicates the region with $\alpha = 2$ and the vertical dashed line indicates the cut region for the bottom panel. Bottom panel: the black line represents a vertical cut of the spectral index through the centre of the image, for the face-on RHD model shown above, and the blue line represents the brightness distribution along the same cut for the 3 mm simulated observation, without convolution with the ALMA beam. The angular offset is measured with respect to the centre of the map.

towards source B. This would also suggest that source B might have formed out of a core with initial turbulence or perturbation instead of solid-body rotation, which would be in agreement with the different orientations of the structures and rotation axes for sources A and B (Pineda et al. 2012; Maureira et al. 2020), similar to what has been suggested for other close Class 0 multiple systems (Hara et al. 2021).

Another possibility not involving spiral arms would be that the position of the continuum is not tracing the position of the protostar. For instance, in the distribution of the spectral index shown in Fig. 1, the minimum value is fairly close to the centre of the overall structure, while the peak of the dust continuum emission is not. This difference may be due to the continuum peak tracing instead the position of a hot structure close to the protostar and not the protostar itself, which would also be supported by the asymmetric distribution of the complex organic molecule emission (Calcutt et al.

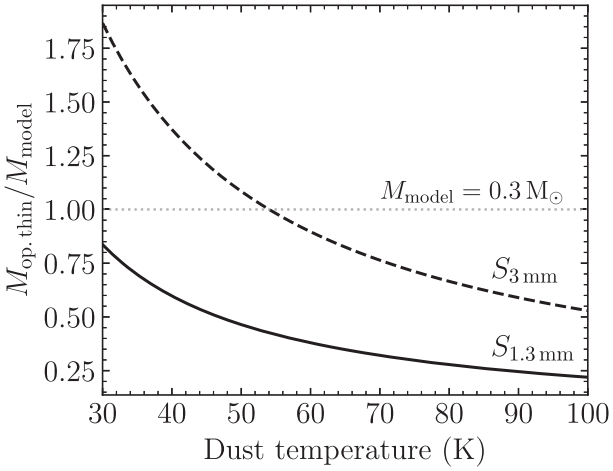


**Figure 11.** Ratio of the observational mass estimates over the original disc mass, for the RHD model. Masses are derived using equation (1) from the flux densities at 1.3 and 3 mm. The figure shows that the mass is best estimated for a dust temperature of 55 K with the less optically thick emission, i.e. at 3 mm.

2018a, b; Manigand et al. 2020, 2021). This asymmetry could also be associated with asymmetric accretion from the envelope on to the disc, based on the previous detection of infalling material in source B (Pineda et al. 2012; Zapata et al. 2013). Follow-up observations with similarly high angular resolutions at longer wavelengths (e.g. VLA observations) would be helpful to further assess the origin of the asymmetry.

### 6.6 Mass estimates under the optically thin approximation

The masses of observed discs are generally calculated assuming that the dust emission is optically thin. However, as previously discussed, the model that best reproduces our observations is highly optically thick. Therefore, similar to the analysis done by Evans et al. (2017), we investigate here how much are the masses under- or overestimated in the case of embedded discs, when using this common approach.

The mass of a disc can be estimated from its flux density using the following equation (Hildebrand 1983):

$$M_{\mathrm{disk}} = \frac{g S_\nu d^2}{\kappa_\nu B(T_{\mathrm{dust}})}, \quad (1)$$

where $S_\nu$ is the flux, $g$ is the gas-to-dust mass ratio of 100, $d$ is the distance, $\kappa_{1.3\,\mathrm{mm}} = 1.50\,\mathrm{cm^2\,g^{-1}}$ and $\kappa_{3\,\mathrm{mm}} = 0.58\,\mathrm{cm^2\,g^{-1}}$ are the dust opacities and $B(T_{\mathrm{dust}})$ is the Planck function for a given dust temperature $T_{\mathrm{dust}}$. The fluxes of the RHD model integrated over a $5\,\sigma$ region are $S_{1.3\,\mathrm{mm}} = 1.60\,\mathrm{Jy}$ and $S_{3\,\mathrm{mm}} = 0.29\,\mathrm{Jy}$. Fig. 11 shows the resultant masses as a fraction of the true mass ($0.3\,\mathrm{M}_\odot$) for temperatures from 30 K to 100 K. As the figure shows, although the disc temperatures are high, at least 100 K in the mid-plane (Fig. 5), when using the optically thin approximation at 1.3mm, the measured mass is closer to the real value for lower temperatures (∼30 K). When assuming higher temperatures, the best estimates are obtained when using the 3 mm fluxes. For this particular disc model, using the 3 mm fluxes and a dust temperature of 55 K result in a more accurate estimate. This analysis shows that one can obtain a reasonable mass estimate under two erroneous assumptions (optically thin and low temperatures) due to the two effects cancelling out each other. We caution the reader that the selection of this temperature works best

Downloaded from https://academic.oup.com/mnras/article/508/2/2583/6372913 by University of Leeds user on 28 June 2022

for this particular model but it is not necessarily meant to be used for all kind of embedded discs.

## 7 CONCLUSIONS

In this work, we presented continuum ALMA observations at 1.3 and 3 mm towards the Class 0 protostar IRAS 16293−2422B with resolutions of 88 mas (∼12 au) and 46 mas (∼6.5 au), respectively. We analysed profiles of brightness distribution and provide a spectral index map. We compared these with MHD and RHD numerical simulations of a gravitationally unstable disc with masses of 0.1 and 0.3 $M_\odot$, respectively, both formed following the collapse of a dense core. Our results can be summarized as follows:

(i) The peak brightness temperatures at 1.3 and 3 mm are 290 and 470 K, respectively. Both peaks appear shifted to the west with respect to the centre of the more extended emission which extends up to $r \sim 46$ au at 3 mm. The spectral index decreases towards the centre, starting from ∼3 and reaching values less than 2 in the inner ∼ 20 au.

(ii) We performed dust radiative transfer calculations and synthetic observations assuming maximum grain sizes of $a_{\rm max} = 1$ and 10 μm for the two disc models. For these opacities, the albedo of the dust grains is very low and therefore the continuum flux arises mainly from thermal dust emission. The observed fluxes at both wavelengths can be better reproduced with the RHD disc assuming $a_{\rm max} = 10$ μm. This model has higher dust temperatures ranging from 200 to 400 K across the disc mid-plane. These higher temperatures are naturally achieved by the numerical simulation that includes radiative transfer coupled with additional heating from the compression triggered by the spiral arms.

(iii) Radiative heating from the central protostar alone is not able to heat up the dust beyond a few au from the central source and thus, cannot reproduce the high observed brightness temperatures (100–200 K) between ∼15 and 30 au. These results still hold when increasing the luminosity of the central source or changing the dust opacities.

(iv) The presence of spiral arms in the RHD model leads to asymmetries in the brightness profiles beyond the peak. These asymmetries resemble the observed ones and thus we speculate spiral the structures could be present in this particular source.

(v) Both disc models reproduce well the low spectral index values and its spatial distribution. This is because both discs are optically thick and show temperatures that are higher in the inner layers compared with the outer layers (i.e. self-obscuration). Thus, low spectral index values in embedded discs can naturally arise due to these discs being optically thick and with an increasing temperature towards the inner layers (including the mid-plane) unlike the more evolved protoplanetary discs at comparable scales. This scenario does not require mm grain sizes or self-scattering effects.

The high temperatures present in the disc around source B allow to explain the large variety of complex organic molecules observed in the hot corino IRAS 16293−2422, as reported by recent spectral lines studies, such as the PILS survey. The possibility that these high temperatures are the consequence of gravitational instabilities, points to the idea that self-gravitating discs may provide the conditions for the detection of hot corinos in Class 0 sources. Thus, future observational and modelling studies targeting emission of COMs in gravitationally unstable discs may help to test this scenario.

Future high-resolution continuum observations at different wavelengths are needed to further investigate density and temperature substructures present in the disc. Similarly, future multiwavelength high-resolution observations are necessary to investigate if the temperature and density distribution models presented in this work can also explain the fluxes and spectral index behaviour for other embedded discs, providing important observational constraints to the physical structure of young protostellar discs.

## ACKNOWLEDGEMENTS

JZ, MJM, BZ, and PC acknowledge the financial support of the Max Planck Society. HBL is supported by the Ministry of Science and Technology, Taiwan (MOST; Grant No. 108-2112-M-001-002-MY3). JDI acknowledges support from the Science and Technology Facilities Council of the United Kingdom (STFC) under ST/T000287/1. We also thank Jaime E. Pineda, Munan Gong, Dominique Segura-Cox, and Kedron Silsbee for fruitful discussions about this project.

This paper makes use of ALMA data from the following projects: 2017.1.01247.S (PI: G. Dipierro) and 2016.1.00457.S (PI: Y. Oya). ALMA is a partnership of ESO (representing its member states), NSF (USA) and NINS (Japan), together with NRC (Canada), MOST and ASIAA (Taiwan), and KASI (Republic of Korea), in cooperation with the Republic of Chile. The Joint ALMA Observatory is operated by ESO, AUI NRAO, and NAOJ. The National Radio Astronomy Observatory is a facility of the National Science Foundation operated under cooperative agreement by Associated Universities, Inc. This research made use of APLPY, an open-source plotting package for PYTHON (Robitaille & Bressert 2012) hosted at http://aplpy.github.io and MAYAVI (Ramachandran & Varoquaux 2011), an open-source library for 3D rendering in PYTHON hosted at https://docs.enthought.com/mayavi/mayavi.

## DATA AVAILABILITY

The data underlying this article will be shared on reasonable request to the corresponding author.

## REFERENCES

Akiyama E., Vorobyov E. I., Baobabu Liu H., Dong R., de Leon J., Liu S.-Y., Tamura M., 2019, AJ, 157, 165
Andre P., Ward-Thompson D., Barsony M., 1993, ApJ, 406, 122
Andre P., Ward-Thompson D., Barsony M., 2000, in Mannings V., Boss A. P., Russell S. S., eds, Protostars and Planets IV. The Univ. Arizona Press, Tucson, AZ, p. 59,
Armitage P. J., 2009, Astrophysics of Planet Formation. Cambridge Univ. Press, New York
Armitage P. J., 2011, ARA&A, 49, 195
Bate M. R., Bonnell I. A., Price N. M., 1995, MNRAS, 277, 362
Blake G. A., van Dishoeck E. F., Jansen D. J., Groesbeck T. D., Mundy L. G., 1994, ApJ, 428, 680
Bodenheimer P., Yorke H. W., Rozyczka M., Tohline J. E., 1990, ApJ, 355, 651
Bohren C. F., Huffman D. R., 1983, Absorption and Scattering of Light by Small Particles. Wiely, New York
Boley A. C., Durisen R. H., 2008, ApJ, 685, 1193
Boley A. C., Mejía A. C., Durisen R. H., Cai K., Pickett M. K., D'Alessio P., 2006, ApJ, 651, 517
Boss A. P., 2009, ApJ, 694, 107
Brunngräber R., Wolf S., 2018, A&A, 611, A90
Brunngräber R., Wolf S., 2020, A&A, 640, A122
Calcutt H. et al., 2018a, A&A, 616, A90
Calcutt H. et al., 2018b, A&A, 617, A95
Cazaux S., Tielens A. G. G. M., Ceccarelli C., Castets A., Wakelam V., Caux E., Parise B., Teyssier D., 2003, ApJ, 593, L51



Downloaded from https://academic.oup.com/mnras/article/508/2/2583/6372913 by University of Leeds user on 28 June 2022

Ceccarelli C., Castets A., Loinard L., Caux E., Tielens A. G. G. M., 1998, A&A, 338, L43
Ceccarelli C., Loinard L., Castets A., Tielens A. G. G. M., Caux E., 2000, A&A, 357, L9
Chandler C. J., Brogan C. L., Shirley Y. L., Loinard L., 2005, ApJ, 632, 371
Chiang E. I., Goldreich P., 1997, ApJ, 490, 368
Cornwell T. J., 2008, IEEE J. Sel. Top. Signal Process., 2, 793
Coutens A., Commerçon B., Wakelam V., 2020, A&A, 643, A108
Crimier N., Ceccarelli C., Maret S., Bottinelli S., Caux E., Kahane C., Lis D. C., Olofsson J., 2010, A&A, 519, A65
Dartois E., Dutrey A., Guilloteau S., 2003, A&A, 399, 773
Das H. K., Voshchinnikov N. V., Il'in V. B., 2010, MNRAS, 404, 265
De Simone M. et al., 2020, ApJ, 896, L3
Dong R., Vorobyov E., Pavlyuchenkov Y., Chiang E., Liu H. B., 2016, ApJ, 823, 141
Draine B. T., Lee H. M., 1984, ApJ, 285, 89
Draine B. T., Malhotra S., 1993, ApJ, 414, 632
Dullemond C. P., Hollenbach D., Kamp I., D'Alessio P., 2007, in Reipurth B., Jewitt D., Keil K., eds, Protostars and Planets V. The Univ. Arizona Press, Tucson, AZ, p. 555
Dullemond C. P., Küffmeier M., Goicovic F., Fukagawa M., Oehl V., Kramer M., 2019, A&A, 628, A20
Durisen R. H., Boss A. P., Mayer L., Nelson A. F., Quinn T., Rice W. K. M., 2007, in Reipurth B., Jewitt D., Keil K., eds, Protostars and Planets V. The Univ. Arizona Press, Tucson, AZ, p. 607
Dutrey A. et al., 2017, A&A, 607, A130
Dzib S. A. et al., 2018, A&A, 614, A20
Evans M. G., Ilee J. D., Boley A. C., Caselli P., Durisen R. H., Hartquist T. W., Rawlings J. M. C., 2015, MNRAS, 453, 1147
Evans M. G. et al., 2017, MNRAS, 470, 1828
Evans M. G., Hartquist T. W., Caselli P., Boley A. C., Ilee J. D., Rawlings J. M. C., 2019, MNRAS, 483, 1266
Forgan D., Rice K., Stamatellos D., Whitworth A., 2009, MNRAS, 394, 882
Galván-Madrid R., Liu H. B., Izquierdo A. F., Miotello A., Zhao B., Carrasco-González C., Lizano S., Rodríguez L. F., 2018, ApJ, 868, 39
Guilloteau S. et al., 2016, A&A, 586, L1
Hara C. et al., 2021, ApJ, 912, 34
Hernández-Gómez A., Sahnoun E., Caux E., Wiesenfeld L., Loinard L., Bottinelli S., Hammami K., Menten K. M., 2019a, MNRAS, 483, 2014
Hernández-Gómez A. et al., 2019b, ApJ, 875, 94
Hildebrand R. H., 1983, QJRAS, 24, 267
Hsu S.-Y. et al., 2020, ApJ, 898, 107
Ilee J. D., Boley A. C., Caselli P., Durisen R. H., Hartquist T. W., Rawlings J. M. C., 2011, MNRAS, 417, 2950
Ilee J. D. et al., 2017, MNRAS, 472, 189
Jacobsen S. K. et al., 2018, A&A, 612, A72
Jørgensen J. K. et al., 2007, ApJ, 659, 479
Jørgensen J. K., van Dishoeck E. F., Visser R., Bourke T. L., Wilner D. J., Lommen D., Hogerheijde M. R., Myers P. C., 2009, A&A, 507, 861
Jørgensen J. K., Bourke T. L., Nguyen Luong Q., Takakuwa S., 2011, A&A, 534, A100
Jørgensen J. K., Favre C., Bisschop S. E., Bourke T. L., van Dishoeck E. F., Schmalzl M., 2012, ApJ, 757, L4
Jørgensen J. K. et al., 2016, A&A, 595, A117
Jørgensen J. K. et al., 2018, A&A, 620, A170
Kama M., Min M., Dominik C., 2009, A&A, 506, 1199
Kenyon S. J., Hartmann L., 1987, ApJ, 323, 714
Krasnopolsky R., Li Z.-Y., Shang H., 2010, ApJ, 716, 1541
Kratter K., Lodato G., 2016, ARA&A, 54, 271
Kuffmeier M., Reissl S., Wolf S., Stephens I., Calcutt H., 2020, A&A, 639, A137
Labdon A. et al., 2021, A&A, 646, A102
Laor A., Draine B. T., 1993, ApJ, 402, 441
Larson R. B., 1969, MNRAS, 145, 271
Lee C.-F., Li Z.-Y., Yang H., Daniel Lin Z.-Y., Ching T.-C., Lai S.-P., 2021, ApJ, 910, 75
Li J. I.-H., Liu H. B., Hasegawa Y., Hirano N., 2017, ApJ, 840, 72
Lin Z.-Y. D., Lee C.-F., Li Z.-Y., Tobin J. J., Turner N. J., 2021, MNRAS, 501, 1316
Liu H. B., 2019, ApJ, 877, L22
Liu H. B., Hasegawa Y., Ching T.-C., Lai S.-P., Hirano N., Rao R., 2018, A&A, 617, A3
Liu H. B. et al., 2019, ApJ, 884, 97
Lizano S., Tapia C., Boehler Y., D'Alessio P., 2016, ApJ, 817, 35
Loinard L., Rodríguez L. F., D'Alessio P., Wilner D. J., Ho P. T. P., 2002, ApJ, 581, L109
Loinard L., Chandler C. J., Rodríguez L. F., D'Alessio P., Brogan C. L., Wilner D. J., Ho P. T. P., 2007, ApJ, 670, 1353
Machida M. N., Inutsuka S.-I., Matsumoto T., 2011, ApJ, 729, 42
Manigand S. et al., 2020, A&A, 635, A48
Manigand S. et al., 2021, A&A, 645, A53
Mathis J. S., Rumpl W., Nordsieck K. H., 1977, ApJ, 217, 425
Maureira M. J., Pineda J. E., Segura-Cox D. M., Caselli P., Testi L., Lodato G., Loinard L., Hernández-Gómez A., 2020, ApJ, 897, 59
Maury A. J. et al., 2019, A&A, 621, A76
Miotello A., Testi L., Lodato G., Ricci L., Rosotti G., Brooks K., Maury A., Natta A., 2014, A&A, 567, A32
Ohashi N., Hayashi M., Ho P. T. P., Momose M., 1997, ApJ, 475, 211
Ossenkopf V., 1991, A&A, 251, 210
Ossenkopf V., Henning T., 1994, A&A, 291, 943
Oya Y., Yamamoto S., 2020, ApJ, 904, 185
Oya Y., Sakai N., Lefloch B., López-Sepulcre A., Watanabe Y., Ceccarelli C., Yamamoto S., 2015, ApJ, 812, 59
Oya Y., Sakai N., López-Sepulcre A., Watanabe Y., Ceccarelli C., Lefloch B., Favre C., Yamamoto S., 2016, ApJ, 824, 88
Oya Y. et al., 2018, ApJ, 854, 96
Paneque-Carreño T. et al., 2021, ApJ, 914, 88
Pineda J. E. et al., 2012, A&A, 544, L7
Pineda J. E., Segura-Cox D., Caselli P., Cunningham N., Zhao B., Schmiedeke A., Maureira M. J., Neri R., 2020, Nat. Astron., 4, 1158
Quénard D., Ilee J. D., Jiménez-Serra I., Forgan D. H., Hall C., Rice K., 2018, ApJ, 868, 9
Rao R., Girart J. M., Marrone D. P., Lai S.-P., Schnee S., 2009, ApJ, 707, 921
Ramachandran P., Varoquaux G., 2011, Comput. Sci. Engineering, 13, 40
Rau U., Cornwell T. J., 2011, A&A, 532, A71
Reissl S., Wolf S., Brauer R., 2016, A&A, 593, A87
Robitaille T., Bressert E. 2012, Astrophysics Source Code Library, record ascl:1208.017
Rodríguez L. F., Loinard L., D'Alessio P., Wilner D. J., Ho P. T. P., 2005, ApJ, 621, L133
Schöier F. L., Jørgensen J. K., van Dishoeck E. F., Blake G. A., 2002, A&A, 390, 1001
Segura-Cox D. M. et al., 2018, ApJ, 866, 161
Sierra A., Lizano S., 2020, ApJ, 892, 136
Silsbee K., Ivlev A. V., Sipilä O., Caselli P., Zhao B., 2020, A&A, 641, A39
Stamatellos D., Whitworth A. P., Bisbas T., Goodwin S., 2007, A&A, 475, 37
Stark R. et al., 2004, ApJ, 608, 341
Takakuwa S. et al., 2007, ApJ, 662, 431
Tapia C., Lizano S., 2017, ApJ, 849, 136
Tobin J. J., Hartmann L., Calvet N., D'Alessio P., 2008, ApJ, 679, 1364
Tobin J. J. et al., 2016, Nature, 538, 483
Tobin J. J. et al., 2020, ApJ, 890, 130
Toomre A., 1964, ApJ, 139, 1217
Valdivia V., Maury A., Brauer R., Hennebelle P., Galametz M., Guillet V., Reissl S., 2019, MNRAS, 488, 4897
van der Wiel M. H. D. et al., 2019, A&A, 626, A93
van Dishoeck E. F., Blake G. A., Jansen D. J., Groesbeck T. D., 1995, ApJ, 447, 760
van't Hoff M. L. R., Tobin J. J., Harsono D., van Dishoeck E. F., 2018, A&A, 615, A83
van't Hoff M. L. R., Bergin E. A., Jørgensen J. K., Blake G. A., 2020a, ApJ, 897, L38
van't Hoff M. L. R. et al., 2020b, ApJ, 901, 166
Veronesi B., Paneque-Carreño T., Lodato G., Testi L., Pérez L. M., Bertin G., Hall C., 2021, ApJ, 914, L27
Vorobyov E. I., Basu S., 2010, ApJ, 714, L133
Weingartner J. C., Draine B. T., 2001, ApJ, 548, 296

Downloaded from https://academic.oup.com/mnras/article/508/2/2583/6372913 by University of Leeds user on 28 June 2022

Whitehouse S. C., Bate M. R., 2004, MNRAS, 353, 1078
Whitehouse S. C., Bate M. R., 2006, MNRAS, 367, 32
Woitke P. et al., 2016, A&A, 586, A103
Wolf S., Voshchinnikov N. V., 2004, Comput. Phys. Commun., 162, 113
Wootten A., 1989, ApJ, 337, 858
Xu W., Kunz M. W., 2021b, MNRAS, in press
Zapata L. A., Loinard L., Rodríguez L. F., Hernández-Hernández V., Takahashi S., Trejo A., Parise B., 2013, ApJ, 764, L14
Zhao B., Caselli P., Li Z.-Y., Krasnopolsky R., 2018, MNRAS, 473, 4868

## APPENDIX A: SPECTRAL INDEX

The slope of the spectral energy distribution (namely, the spectral index $\alpha$) in logspace, between $\nu_1$ and $\nu_2$ (for $\nu_1 > \nu_2$), can be obtained as

$$\alpha = \frac{\log(I_1) - \log(I_2)}{\log(\nu_1) - \log(\nu_2)}, \tag{A1}$$

with $I_1$ and $I_2$ the specific intensities at frequencies $\nu_1$ and $\nu_2$, respectively. In the Rayleigh–Jeans regime, the relation between the intensity and the brightness temperature $T_\mathrm{b}$ at frequency $\nu$ is given by

$$I_\nu = \frac{2k_\mathrm{B}}{c^2}\nu^2\, T_\mathrm{b}, \tag{A2}$$

with $k_\mathrm{B}$ the Boltzmann constant. Since $I \propto \nu^2 T_\mathrm{b}$, then equation (A1) can be expressed as

$$\alpha = \frac{\log\left(\nu_1^2\, T_{\mathrm{b},1}\right) - \log\left(\nu_2^2\, T_{\mathrm{b},2}\right)}{\log\left(\nu_1\right) - \log\left(\nu_2\right)}, \tag{A3}$$

$$= \frac{2\log\left(\frac{\nu_1}{\nu_2}\right)}{\log\left(\frac{\nu_1}{\nu_2}\right)} + \frac{\log\left(\frac{T_{\mathrm{b},1}}{T_{\mathrm{b},2}}\right)}{\log\left(\frac{\nu_1}{\nu_2}\right)}, \tag{A4}$$

$$= 2 + \frac{\log(T_{\mathrm{b},1}) - \log(T_{\mathrm{b},2})}{\log(\nu_1) - \log(\nu_2)}, \tag{A5}$$

thus,

$$T_{\mathrm{b},1} \begin{cases} \geqslant T_{\mathrm{b},2} & , \ \alpha \geqslant 2 \\ < T_{\mathrm{b},2} & , \ \alpha < 2 \ . \end{cases}$$

This last inequality tells us that a spectral index observed to be lower than 2 means that the brightness temperature at higher frequency is lower than at lower frequency, which is the opposite to what is expected for a blackbody radiator at a single temperature. In our observations this low value of $\alpha$ can be explained by the two wavelengths tracing optically thick ($T_\mathrm{b} \lesssim T_\mathrm{BB}$) layers at different temperatures. Moreover, since the opacity in the Rayleigh–Jeans regime decreases as a function of frequency ($\kappa \propto \nu^{\alpha-2}$), then the surface at $\tau = 1$ traced by the 3 mm observation lies deeper into the disc as compared to that traced at 1.3 mm. This is indicative of the inner regions of the disc being warmer than the outer regions.

## APPENDIX B: SPECTRAL INDEX FOR THE MHD DISC MODEL

To complement the analysis presented in Section 5.2, we have also generated the 1.3 mm, 3 mm and spectral index maps for the MHD disc formation model described in Section 3.1.1. The results are shown in Fig. B1 in the same layout as Figs 1 and 7. We observed a similar tendency as compared to the RHD model in which the spectral index falls to around 1.8 towards the densest parts of the model. This implies that both models, considered in this study, are capable of reproducing the low values of $\alpha$ expected from early discs with a mid-plane at higher temperatures than the outer layers.

## APPENDIX C: TOOMRE $Q$ PARAMETER FOR BOTH DISC MODELS

In Fig. C1, we show the Toomre parameter for the two disc models considered here, the RHD and MHD disc. Both discs are gravitationally unstable and susceptible to non-axisymmetric perturbations in

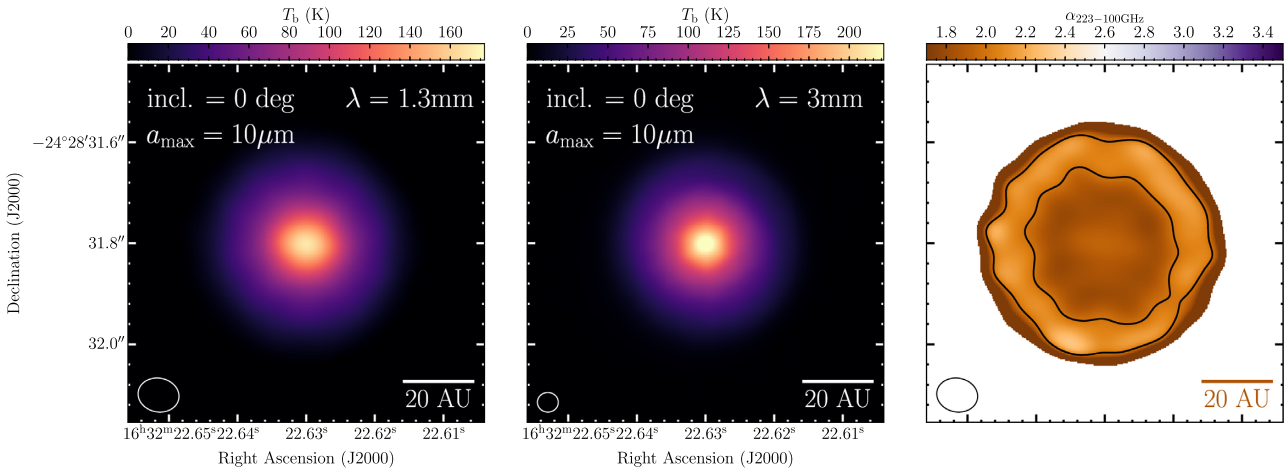


**Figure B1.** Synthetic brightness temperature maps at 1.3 and 3 mm along with the spectral index for the MHD disc formation model from Zhao et al. (2018), described in Section 3.1.1. A similar behaviour is observed as compared to the RHD gravitationally unstable model, in which the spectral index ($\alpha$) is observed to decrease towards the centre of the disc. The contours in the rightmost panel indicate $\alpha = 1.7$ and 2, inside-out.

Downloaded from https://academic.oup.com/mnras/article/508/2/2583/6372913 by University of Leeds user on 28 June 2022

the regions where $Q \lesssim 1.7$ (Durisen et al. 2007), which is between 7 and 20 au for the RHD disc and between 8 and 25 au for the MHD, with a small exception within a radius of 15–22 au, but still remaining under $Q = 2$. In spite of the spiral arms being prominent in only one of the two models (RHD), both disc are actually gravitationally unstable.

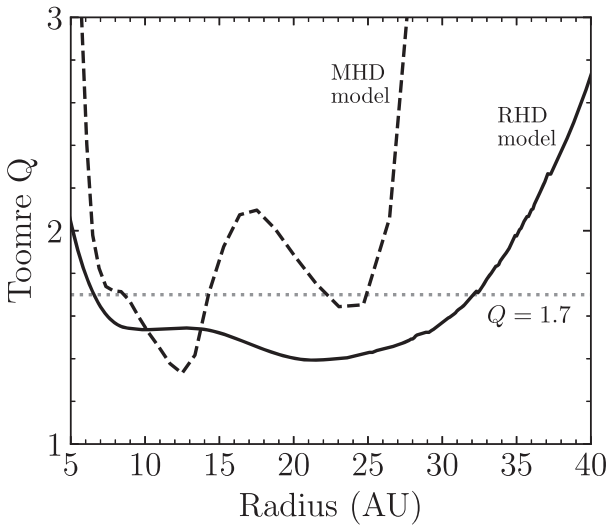


**Figure C1.** Toomre Q parameter of both disc models. The RHD model has a Q$\lesssim$ 1.7 at radii larger than 7 au, with a minimum value of 1.4 at 20 au. The MHD disc also reach values lower than 1.7 between 8 and 25 au. In spite of the spiral arms being prominent in only one of the two models (RHD), both disc are actually gravitationally unstable.

This paper has been typeset from a TEX/LATEX file prepared by the author.

Downloaded from https://academic.oup.com/mnras/article/508/2/2583/6372913 by University of Leeds user on 28 June 2022